

An Enclosed One Wheel Robot

B.Tech. Project Final Report

By

Joydeep Biswas

Roll No. 04026010

Under the guidance of

Professor B. Seth (Department of Mechanical Engineering)

Professor S. Umasankar (Department of Physics)



Department of Physics
Indian Institute of Technology
April 2008

Acknowledgements

I would like to thank Professor Bharatendu Seth and Professor Umashankar for their guidance and encouragement, and the valuable time they spent discussing the issues of the project with me.

I would like to specially thank Professor Amarnath for fathering the technical activities in the institute and under UMIC. Sir, without your support and encouragement to go ahead and try out every singly wacky idea, we probably wouldn't have known the "T" of Technology!

I am extremely grateful to Professor Mahajan for his support and help in getting the mechanical components fabricated in the Physics Department Workshop.

The members of the staff over at the Physics Department Workshop deserve a huge part of the credit for the mechanical construction of the robot. Their dedication to the dimensional accuracy and finish of every small part is really laudable.

Index

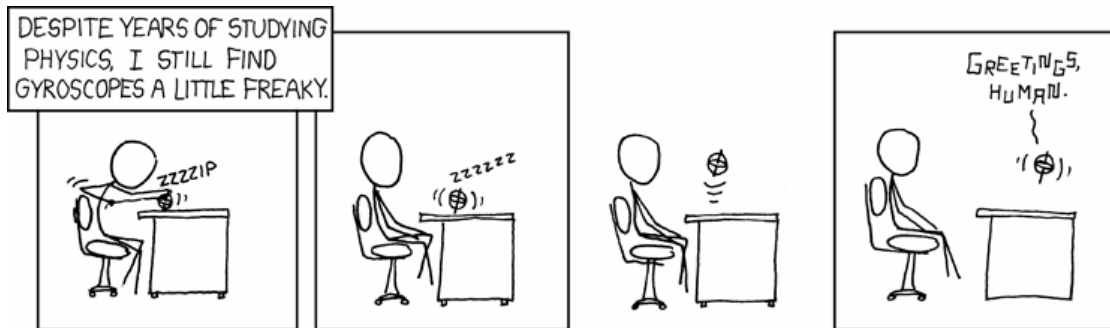
1. INTRODUCTION	5
2. OVERVIEW	7
3. PREVIOUS WORK	8
4. THE REACTION WHEEL INVERTED PENDULUM	9
5. SIMULATION OF THE REACTION WHEEL INVERTED PENDULUM	11
6. ONE WHEEL ROBOT CONFIGURATIONS.....	15
THE UNICYCLE CONFIGURATION	15
THE OPEN WHEEL CONFIGURATION	16
THE ENCLOSED WHEEL CONFIGURATION.....	17
7. MATHEMATICS OF THE ONE WHEEL ROBOT	18
COORDINATE FRAME DEFINITIONS.....	18
EULER ANGLE DEFINITIONS FOR THE SYSTEM.....	19
AXIS TRANSFORMATIONS.....	19
THE STATE ESTIMATOR	20
8. COMPONENT SELECTION	22
REACTION WHEEL, REACTION WHEEL MOTOR.....	22
DRIVE MOTOR	22
BATTERIES.....	22
9. INERTIAL MEASUREMENT UNIT FILTERING	24
10. MECHANICAL CONSTRUCTION	29
11. TEST RIG	31
12. ELECTRONICS	32
THE INERTIAL MEASUREMENT UNIT (IMU).....	32
THE MICROCONTROLLER AND WIRELESS LINK	32
THE MOTOR DRIVERS	32
THE USB ZIGBEE MODULE.....	33
13. TELEMETRY AND CONTROL.....	34
14. CONTROL SYSTEM	35

15. CONCLUSION AND OUTLOOK.....	42
16. REFERENCES	43
APPENDIX A: MOTOR, GEARBOX, ENCODER DATASHEETS.....	44
APPENDIX B: ELECTRONIC COMPONENTS DATASHEETS	49
APPENDIX C: MAC71XX DEVELOPMENT TOOL CHAIN.....	60
APPENDIX D: SOURCE CODE.....	61
MATHEMATICA SOURCE CODE FOR THE SIMULATION OF A REACTION WHEEL INVERTED PENDULUM	61
MATLAB SOURCE CODE FOR IMU FILTER SIMULATION	62
TARGET SOURCE CODE	63

1. Introduction

Anyone who has participated in a slow cycling race would know how difficult it is to balance a statically unstable system at low speeds, without the gyroscopic effect to help out. Now imagine having to balance a stationary cycle, and the problem becomes apparent.

Counter-intuitive as it may seem, such systems can actually be balanced quite simply, without having to disobey the laws of physics. This is where the mechanical gyroscope comes in. A heavy metal disc, once set spinning, resists any change in the orientation of its spin axis. This effect has dazzled physicists for years, and simplified analyses of restricted motions of the gyroscope have given some insight into the laws governing its motion. A complete physical model that exhibits all the intricate behaviours of a spinning wheel is quite involved, since the behaviour of the gyroscope is quite different under different conditions. A physics student who had probably seen his own share of gyroscopic effects succinctly conveys his cowed respect for the powers of the gyroscope in the web comic, xkcd[1]:



Although levitating gyroscopes are probably a few years away, the gyroscopic effect nevertheless does wonders to stabilise systems like the cycle and a single rolling wheel.

A single wheel vehicle could have either of two possible types of configurations. In one, the centre of mass of the system is higher than the wheel axle, so both the “roll” and the “pitch” angles are unstable. A unicycle is just such a system, where the rider tries to maintain the “roll” angle by balancing hand movements, and the “pitch” angle by cycling forward and back as required. A single wheel vehicle with the centre of mass lower than the wheel axle is stabilised in the “pitch” direction, much like a bicycle where the two wheel configuration actually restricts any change in pitch. The “roll” is however still unstable.

Drawing the analogy of the unicyclist balancing himself by flailing his arms about, a single wheel robot could be balanced in much the same way. In essence, the raising and lowering of opposite outstretched arms imparts a counter torque to the body, which helps it to maintain balance. However, to the rider, it is important that the arms return to their horizontal mean position, else after some time, he'd certainly lose balance! This problem is easily solved by using a reaction wheel instead of arms to impart this counter torque. Since the reaction wheel is symmetric about its axis, there really isn't any need to bring it back to its initial angle, thus simplifying matters.

These systems, where the centre of mass is actually higher than the pivot point, can be classified under the category of inverted pendulums. Some systems, like the unicycle, are dual axis inverted pendulum systems, whereas others like a vertical upright plate hinged at the base are single axis. The taller an inverted pendulum, the easier it is to balance it since the moment of inertia and time constant increase with height. Thus, it would require slower responses to balance a tall inverted pendulum, which is why it is easier. It's easier to balance

an upright cricket bat on the palm of one's hand than an upright matchstick on one's finger! However, the taller a system gets, greater is the torque that is required to balance it for the same angular offset. Balancing a cricket bat from an initial tilt of fifteen degrees is considerably simpler than balancing a tall metal pipe from the same initial angle - the latter would require considerable running around!

A balancing stationary upright wheel is analogous to an inverted pendulum. The only difference is that here the pivot (the contact between the wheel and the ground) is fixed, and cannot move in the direction perpendicular to the pivot axis (a wheel cannot move sideways without slipping). Thus, any of the techniques used to balance a stationary inverted pendulum could be used to stabilise the stationary wheel too.

The motivation behind the development of an enclosed single wheel robot is manifold. First, its construction would allow a single wheel robot to travel over most obstacles more easily than other vehicles of the same size. Second, since the entire unit is enclosed within one shell, there are no protruding parts which could snag on obstructions. Theoretically, if the seals could be made water-tight, the vehicle could be used underwater too. Finally, it would also be an interesting learning experience to dynamically stabilize this unusual system.

Through my final year project, I intend to design a single wheel robot capable of balancing itself even while at rest. The entire robot would be enclosed within the wheel, which would rest on a thin rim. The single wheel robot would be balanced by means of a reaction wheel.

2. Overview

The main hurdle in the development of a single wheel robot (as with most other dynamically stable systems) is to ensure that the robot is capable of balancing on its own while at rest. The robot should be able to estimate its equilibrium position without user intervention, and should be resilient to external perturbations as well as changes in its own mass distribution. Therefore, considerable time was spent during the project to achieve this goal alone. Once the robot is capable of balancing itself while at rest, it would be relatively simple to balance it while in motion, since it would be assisted by the gyroscopic effect of the rolling wheel.

This report starts out by briefly reviewing previous work in the field of dynamic balancing in general, and inverted pendulums and single wheel robots in particular.

Since the centre of mass of the single wheel robot (in the chosen configuration) is lower than the main wheel axle, the system is stable along the pitch axis. The behaviour along the roll axis is the same as that of an inverted pendulum. Therefore, to gain a better insight into the dynamics governing the balancing of the single wheel robot, a section (“The Reaction wheel Inverted Pendulum”) has been devoted to deriving the equations that govern its motion. It turns out that deriving the closed form expressions for the reaction wheel inverted pendulum using a given control loop is quite involved. Therefore, rather than deriving the analytical equations of motion, only some numerical simulations were carried out to test the feasibility of balancing an inverted pendulum system using a reaction wheel (“Simulation of the Reaction Wheel Inverted Pendulum”).

Three possible configurations of a single wheel robot were considered and finally the enclosed wheel configuration was chosen, as discussed in the chapter 6, “One Wheel Robot Configurations”.

The implementation has been split into a number of sections. Chapter 7 provides the definitions for the axis conventions used, and the mathematics involving the state estimator. This is followed up by a section discussing the selection of certain key components in Chapter 8. Chapter 9 discusses the development of a complimentary filter to estimate the angles by the IMU. Chapters 10 and 11 describe the mechanical construction of the one wheel robot and the test rig. Chapter 12 is dedicated to the electronic systems developed. Chapter 13 involves the description of the ground station telemetry and control software developed. The control system used to balance the system is described in Chapter 14, along with experimental results. The report concludes with a review of the findings and intended future work on this project.

3. Previous Work

Considerable work has already been done to develop dynamically stable robots stabilised by a variety of mechanisms ranging from robotics arms and linkages to reaction wheels, mechanical gyroscopes and thrusters.

R.C. Hemmings[9] patented a “Velocipede,” a large wheel encircling the rider, powered by hand cranks. A 1935 publication[2] describes the Gyroauto, which carried the riders between a pair of large, side-by-side wheels, and was claimed capable of a speed of 116 mph (187 kph). Also in the same publication[2] is a description of the Dyno-Wheel, a concept having a bus-like chassis straddling a huge central wheel. The relatively large diameter of a single-wheel vehicle enhances its obstacle-crossing ability, smoothness of motion and rolling efficiency[5].

There have been several attempts to make a self balancing unicycle[16, 17, 13, 7, 11], with varying degrees of success. Vos[16] developed a self-contained unicycle that mimicked the behaviour of a human cyclist in maintaining roll and pitch stability. Sumiko Majima and Takashi Kasai[11] developed a unicycle stabilized by a reaction wheel. Zaiquan Sheng et al.[13] developed a mathematical model of a rider riding a unicycle, and used this model itself to determine the construction of a robot that could ride a unicycle. Their robot had a reaction wheel for yaw stabilisation and several momentum transfer linkages for roll stabilisation. Koshiyama and Yamafuji[10] developed a statically stable, single-wheel robot with internal mechanism that could move fore and aft and turn in place; their work emphasized control of the (non-inverted) pendulum carried on the wheel, utilizing momentum transfer in changing direction.

Researchers[6] at the Robotics Institute of Carnegie Melon University have developed an enclosed single wheel robot which is stabilised by an internal mechanical gyroscope. This single wheel robot, named “Gyrover” is stable when it is stationary, and can turn in-place by tilting the mechanical gyroscope. The Gyrover was also demonstrated working underwater. Abdullah Al Mamun et al.[3] from the National University of Singapore have developed a similar enclosed one wheel robot that is again stabilised by means of a mechanical gyroscope.

4. The Reaction wheel Inverted Pendulum

Since the centre of mass of the single wheel robot (in the chosen configuration) is lower than the main wheel axle, the system is stable along the pitch axis. The behaviour along the roll axis is the same as that of an inverted pendulum. Therefore, to gain a better insight into the dynamics governing the balancing of the single wheel robot, this section has been devoted to deriving the equations that govern its motion.

There are numerous ways of stabilising an inverted pendulum like using a base cart[12] or a two wheel system[8] or a reaction wheel[14, 15]. Here I adopt the reaction wheel approach to stabilising an inverted pendulum.

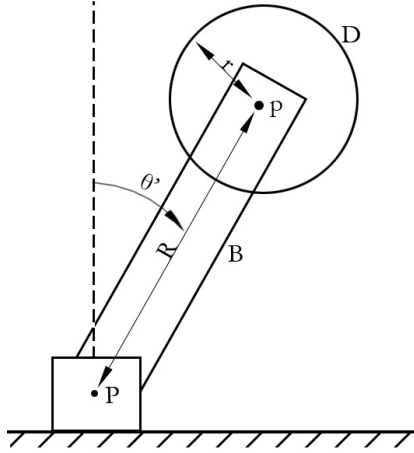


Figure 1: Reaction Wheel Inverted Pendulum

Consider a body “B” which is one block, and a solid disc “D” pivoted on the body so that it can rotate about the pivot “P” which is fixed with respect to the body “B”. The entire body is now pivoted about the point “P”, which is also the origin of the coordinate system. For a body that is not under the effect of any external torques, its net angular momentum is conserved. For a planar geometry and for constrained rotation about the axis perpendicular to the plane alone, this angular momentum conservation gives,

$$\vec{L} = \sum m_i \vec{r}_i \times \vec{v}_i = \text{const.} \quad (1)$$

Here, \vec{L} is the total angular momentum of the system, m_i the point masses that make up the body, \vec{r}_i their respective position vectors, and \vec{v}_i their velocity vectors. However, for the disc, $\vec{r}_i = \vec{r}_{cm} + \vec{r}'_i$ where \vec{r}_{cm} is the position of the centre of mass of the disc, and \vec{r}'_i the position of the point mass from the centre of the disc. For the disc, $\vec{v}_i = \vec{v}_{cm} + \vec{\omega} \times \vec{r}'_i$ where $\vec{\omega}$ is the angular velocity of the disc, and \vec{v}_{cm} is the velocity of the centre of mass of the disc.

$$\vec{L} = \sum_B m_i \vec{r}_i \times \vec{v}_i + \sum_D m_i \vec{r}_i \times \vec{v}_i \quad (2)$$

$$\vec{L} = \sum_B m_i \vec{r}_i \times \vec{v}_i + \sum_D m_i (\vec{r}_{cm} + \vec{r}'_i) \times (\vec{v}_{cm} + \vec{\omega} \times \vec{r}'_i) \quad (3)$$

$$\vec{L} = \vec{L}_B + \sum_D m_i (\vec{r}_{cm} + \vec{r}_i') \times (\vec{v}_{cm} + \vec{\omega} \times \vec{r}_i') \quad (4)$$

$$\vec{L} = \vec{L}_B + \sum_D m_i \vec{r}_{cm} \times \vec{v}_{cm} + \sum_D m_i \vec{r}_{cm} \times (\vec{\omega} \times \vec{r}_i') + \sum_D m_i \vec{r}_i' \times \vec{v}_{cm} + \sum_D m_i \vec{r}_i' \times (\vec{\omega} \times \vec{r}_i') \quad (5)$$

$$\vec{L} = \vec{L}_B + m_D \vec{r}_{cm} \times \vec{v}_{cm} + I_D \vec{\omega} \quad (6)$$

$$\vec{L} = \vec{L}_B + \vec{L}_{D_{cm}} + \vec{L}_{D_\omega} \quad (7)$$

$$\vec{L}_{D_{cm}} = m_D \vec{r}_{cm} \times \vec{v}_{cm}; \vec{L}_{D_\omega} = I_D \vec{\omega} \quad (8)$$

This result implies that the total angular momentum of the body can be expressed as the sum of the angular momentum of the body without the disc and the angular momentum of the disc considering it to be a point mass, and the angular momentum of the disc about its own axis due to its spinning motion. If this body is now subject to external torques, we get,

$$\tau = \frac{d}{dt} \vec{L} = \frac{d}{dt} \vec{L}_B + m_D \frac{d}{dt} (\vec{r}_{cm} \times \vec{v}_{cm}) + I_D \frac{d}{dt} \vec{\omega} \quad (9)$$

This shows that even when there is some net external torque acting on the system, if the angular momentum of the body without the disc and the angular momentum of the disc considering it to be a point mass are to be maintained constant, the disc would have to “absorb” the change in the angular momentum due to the external torque. This is the principle of balancing an inverted pendulum using a reaction wheel.

5. Simulation of the Reaction Wheel Inverted Pendulum

To prove the feasibility of the proposed reaction wheel based balancing system, a series of simple simulations were conducted. These simulations were performed without any control loop, and are just meant to demonstrate that recovery from an initial tilt angle is indeed possible. Hence balancing would be possible with a control system in place.

For the simulation of the reaction wheel inverted pendulum, the following parameters are considered:

1. Distance from P to the centre of mass of B = R'
2. Distance from P to the centre of mass of D = R
3. Angle offset from unstable equilibrium position = θ'

The net external torque acting on the system is given by,

$$\tau = (M_B R' + M_D R) g \sin \theta'$$

Hence,

$$\vec{\tau} = \frac{d}{dt} \vec{L} = \frac{d}{dt} \vec{L}_B + m_D \frac{d}{dt} (\vec{r}_{cm} \times \vec{v}_{cm}) + I_D \frac{d}{dt} \vec{\omega} \quad (10)$$

$$(M_B R' + M_D R) g \sin \theta' \hat{x} = \frac{d}{dt} \vec{L}_B + m_D \frac{d}{dt} (\vec{r}_{cm} \times \vec{v}_{cm}) + I_D \frac{d}{dt} \vec{\omega} \quad (11)$$

$$(M_B R' + M_D R) g \sin \theta' \hat{x} = (M_B R'^2 + M_D R^2) \frac{d}{dt} \omega' + I_D \frac{d}{dt} \omega \quad (12)$$

In reality, ω cannot increase without bounds. ω is limited to the no load speed of the reaction wheel actuator motor, and $\frac{d}{dt} \omega$ by the stall torque of the motor. The product of $\frac{d}{dt} \omega$ and ω is limited by the maximum power output of the motor.

In the implementation of the inverted pendulum system, the value of ω as a function of time depends on the control output of the control system, which is nothing but the voltage supplied to the actuator. By means of the control system, the value of ω is therefore indirectly dependent on the first time integral, time derivative, and time proportional of θ' . Therefore, it would be quite a difficult task to analytically solve for θ' as a function of time. In practice, once the control system for the stabilization of the inverted pendulum has been formulated, the state of the system, given by the variables θ' , ω' and ω is determined by numerical solution.

To check for the maximum angular displacement from which the inverted pendulum can recover, the voltage of the motor is kept constant at the nominal rated value. For this simplified system, an analytical solution for the time variation of θ' is found. An assumption made in the process is that θ' is small, so that the small angle approximations are valid.

Under these conditions, the expression for the reaction wheel angular velocity as a function of time is given by

$$\omega = \frac{\left(1 - e^{-\frac{Ke t}{JKi R}}\right) V}{Ke}$$

J is the reaction wheel moment of inertia, and the motor parameters Ke, Ki and R are described in the system descriptions. In the simulations, the reaction wheel has its mass concentrated at the outer rim, like a ring.

System 1: A Stable System

MicroMo motor 3257, reduction 3.7, values taken from MicroMo datasheet

V (nominal motor voltage) = 24V

Reduction = 3.7

Maximum efficiency = 80%

Back-emf constant, $K_e = 0.174454 \text{ V/rad/s}$

Current constant, $K_i = 7.2973 \text{ A/Nm}$

Terminal resistance, $R = 1.63\Omega$

$M_B = 3\text{kg}$

$M_D = 1\text{kg}$

Radius of inverted pendulum, $R' = 10\text{cm}$

Radius of reaction wheel, $R_d = 6\text{cm}$

In this simulation, the inverted pendulum had an initial offset of 23° , and the offset angle versus time graph shows a concave downward trend, indicating that the inverted pendulum is actually accelerating to the 0° state. Therefore, the system would actually be able to recover from an angle greater than 23° too.

Recovery time = $\sim 0.33\text{s}$

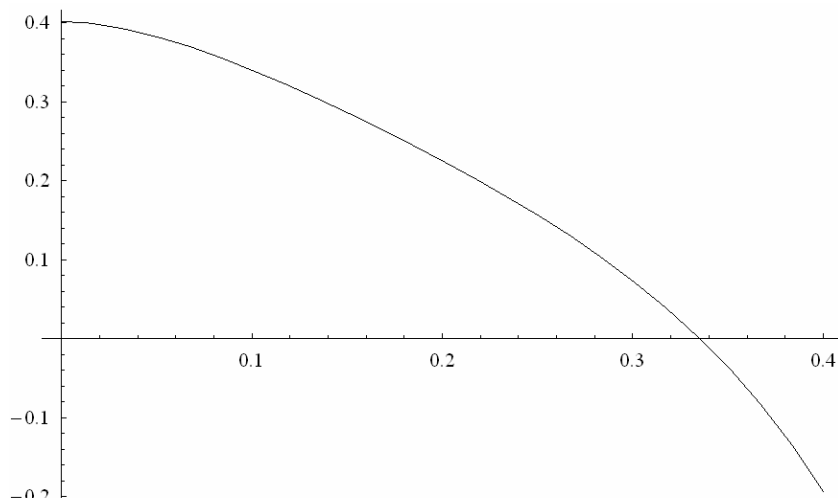


Figure 2: System 1, θ' (rad) vs. t (sec)

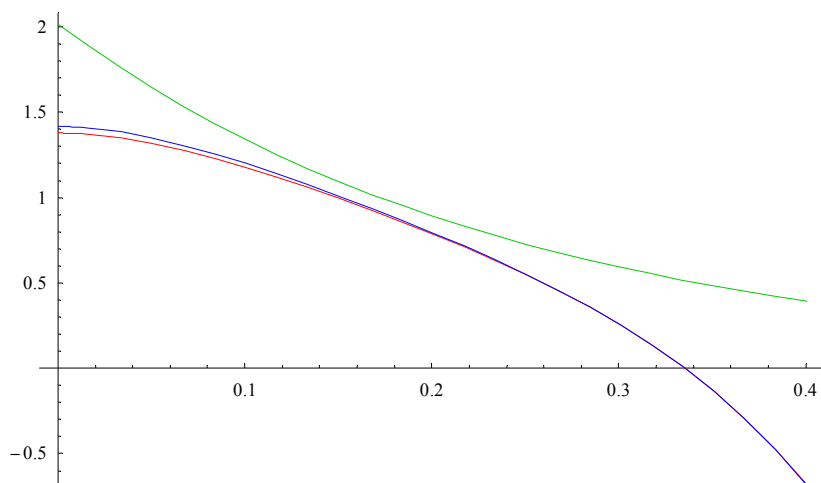


Figure 3: System 1, Torque (Nm) due to gravity (red : exact, blue : small angle approximation), reaction wheel torque (green) (Nm) vs. t (sec)

System 2: Critically Stable System

MicroMo motor 3257, reduction 14, values taken from MicroMo datasheet

V (nominal motor voltage) = 24V

Reduction = 14

Maximum efficiency = 80%

Back-emf constant, $K_e = 0.660095 \text{ V/rad/s}$

Current constant, $K_i = 1.92857 \text{ A/Nm}$

Terminal resistance, $R = 1.63\Omega$

$M_B = 3\text{kg}$

$M_D = 1\text{kg}$

Radius of inverted pendulum, $R' = 10\text{cm}$

Radius of reaction wheel, $R_d = 10\text{cm}$

In this simulation, the inverted pendulum had an initial offset of 40° , and the offset angle versus time graph shows a generally smooth almost linear trend, indicating that the inverted pendulum is moving at an almost constant angular velocity with very little acceleration. Therefore, the system would be close to its limit in this case.

Recovery time = $\sim 0.23\text{s}$

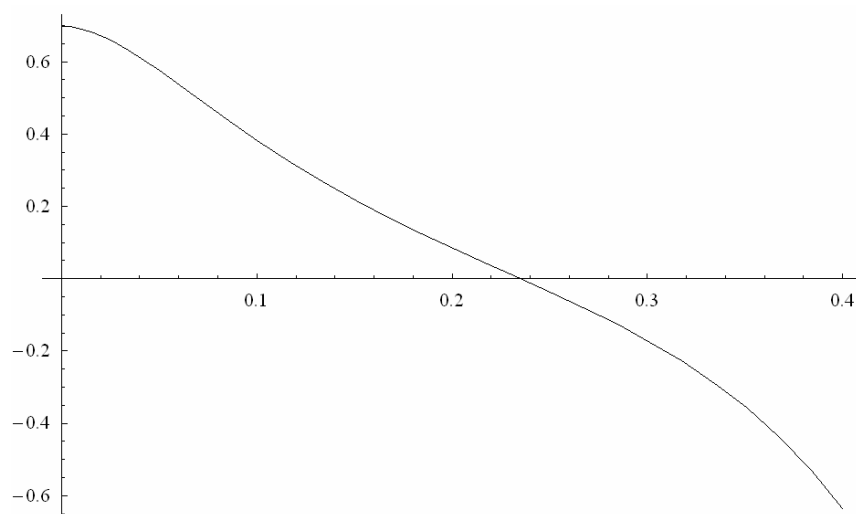


Figure 4: System 2, θ' (rad) vs. t (sec)

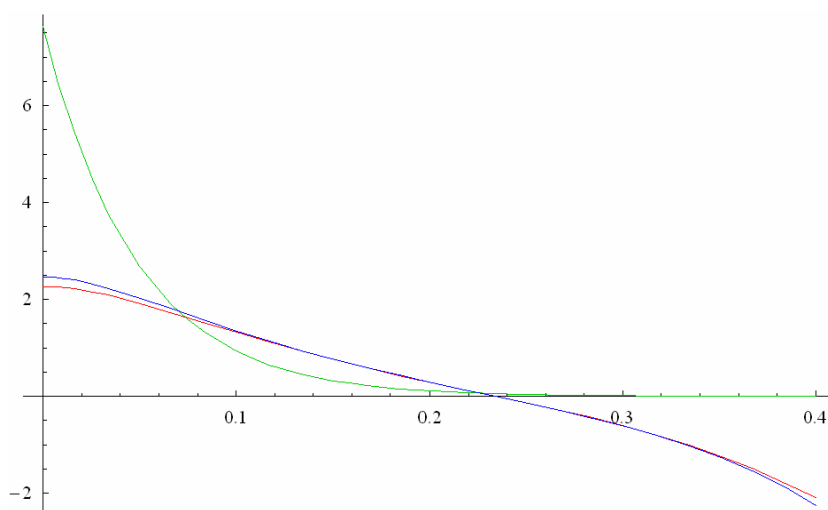


Figure 5: System 2, Torque (Nm) due to gravity (red : exact, blue : small angle approximation), reaction wheel torque (green) (Nm) vs. t (sec)

System 3: A very large inverted pendulum

MicroMo motor 3257, reduction 14, values taken from MicroMo datasheet

V (nominal motor voltage) = 24V

Reduction = 14

Maximum efficiency = 80%

Back-emf constant, $K_e = 0.660095 \text{ V/rad/s}$

Current constant, $K_i = 1.92857 \text{ A/Nm}$

Terminal resistance, $R = 1.63\Omega$

$M_B = 3\text{kg}$

$M_D = 1\text{kg}$

Radius of inverted pendulum, $R' = 100\text{cm}$

Radius of reaction wheel, $R_d = 77.5\text{cm}$

In this simulation, the effects of using a tall inverted pendulum are evident. The recovery time is much longer than in the previous simulations, and the torque required is also much higher. The initial angle of the inverted pendulum was 10° .

Recovery time = $\sim 1.8\text{s}$

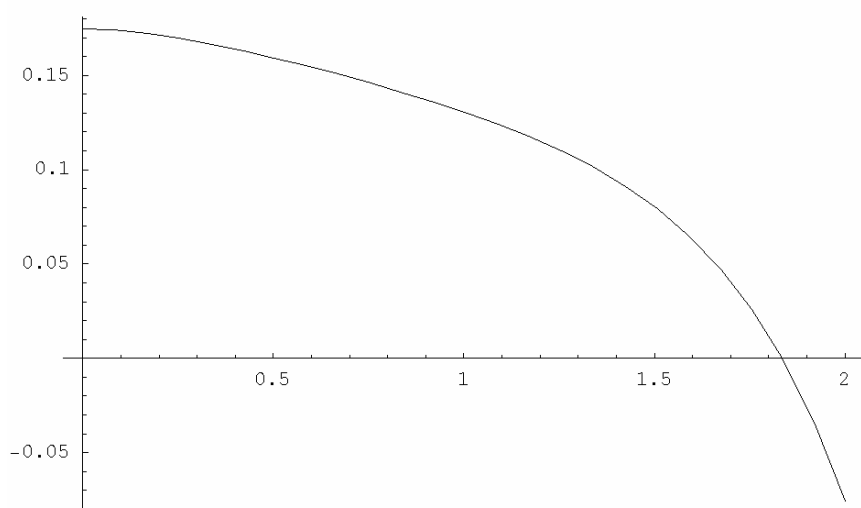


Figure 6: System 3, θ' (rad) vs. t (sec)

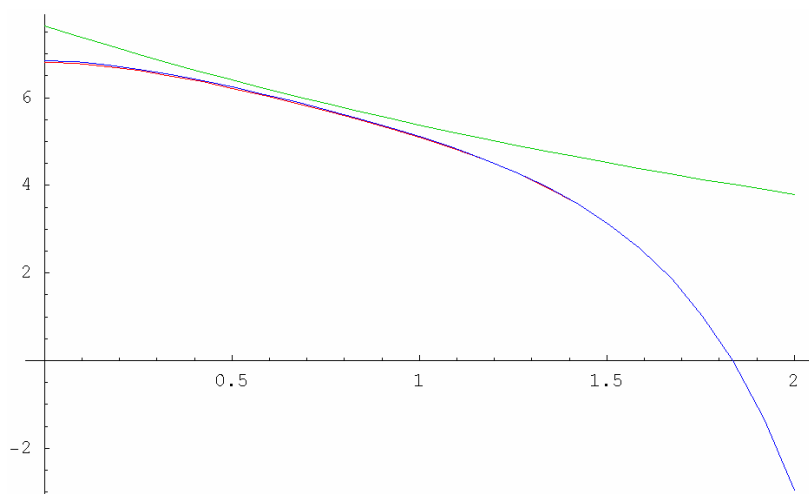


Figure 7: System 3, Torque (Nm) due to gravity (red : exact, blue : small angle approximation), reaction wheel torque (green) (Nm) vs. t (sec)

6. One Wheel Robot Configurations

Three possible configurations of the one wheel robot were considered, each having its own merits and demerits.

The Unicycle Configuration

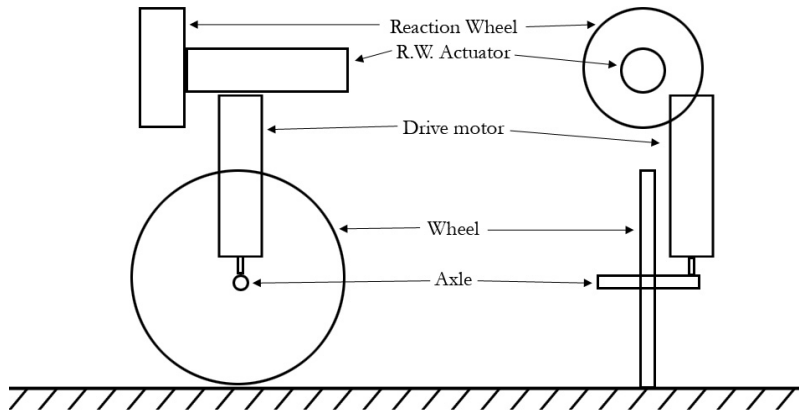


Figure 8: The Unicycle Configuration

In the unicycle configuration, the wheel is the lowest component of the system. For a unicycle, the diameter of the wheel would be considerably less than the total height of the robot. The wheel would be either spoked, like a cycle, or solid to increase its moment of inertia. The centre of mass of the robot would be higher than the axle of the robot, and could even be higher than the highest point of the wheel. The drive motor is aligned vertically, and coupled to the main wheel axle by bevel gears. The reaction wheel, reaction wheel actuator, electronics and batteries are all kept above the wheel.

This system has a rather simple construction, and since all the components are mounted above the wheel, there is no size constraint. Also, since the centre of mass of the system is high, the time constant of the system is larger, so it is relatively easier to stabilise.

The disadvantage is that this system is doubly unstable. Since the centre of mass of the system is above the wheel axle, the robot would be unstable about the pitch axis too. Since the centre of mass of the system is so high, considerable torque would be required to balance the system. This would limit the maximum angle offset from which the robot could recover.

The Open Wheel Configuration

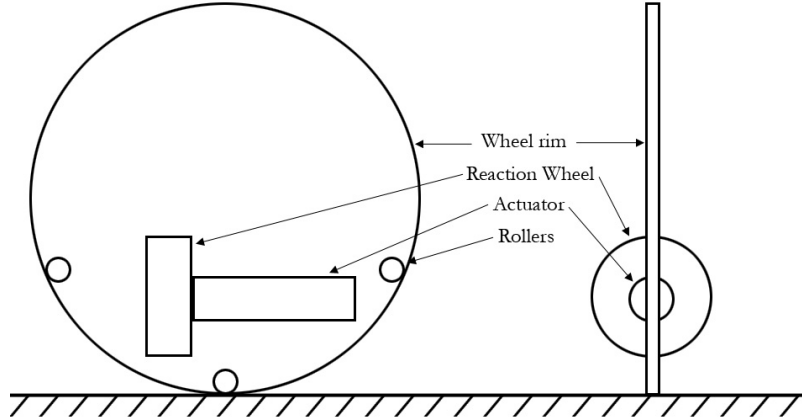


Figure 9: The Open Wheel Configuration

In the open wheel configuration, the “wheel” is actually nothing but a rim. The mechanisms of the robot are kept as close to the ground as possible, on rollers which would roll on the wheel rim.

Since the mechanisms are mounted on rollers inside a wheel rim, there is no size constraint laterally, and the mechanisms could bulge out from the sides without any problems. Further, as the mechanism only requires a rim, the diameter of the rim could be made arbitrarily large without any constraints. This would considerably enhance the obstacle climbing capability of the robot, and make its ride smoother.

The roller and rim design would be rather involved, since the rollers would have to constrain lateral sliding motion between the mechanism and the rim. For this, the rollers could have double helical gear teeth, and the rim matching teeth. This would make the construction of the system rather complex and expensive. The rim would also have to be considerably strong so that it could withstand radial impact forces without deformation. Even the slightest such deformation would cause the rollers to lock up. The alternative to this would be to mount the rollers on a suspension arrangement, making the mechanism even more complex. Also, the bulge of the mechanisms would limit the maximum angle by which the wheel could tilt to one side.

The Enclosed Wheel Configuration

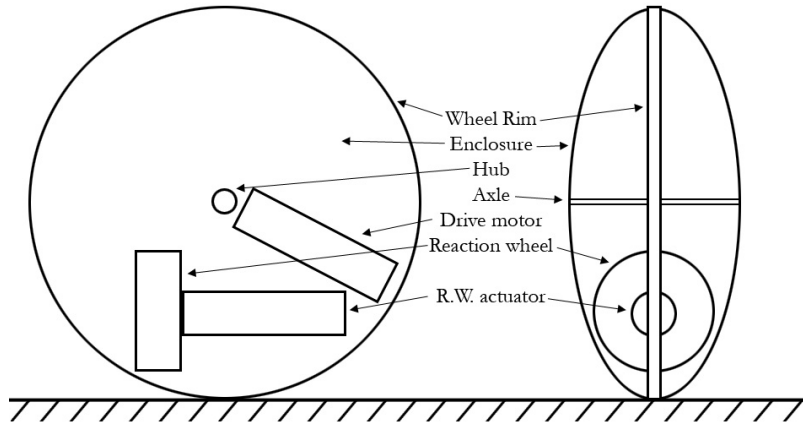


Figure 10: The Enclosed Wheel Configuration

In the enclosed wheel configuration, the entire mass is contained within the shell of the robot. The wheel comprises of a rim, and an enclosing shell. The centre of mass of the system is kept lower than the axle of the wheel. The entire internal mechanism is mounted as a pendulum mass from the axle of the wheel. The electronics and batteries are also attached to this structure.

This system is quite simple to construct. Since the centre of mass is lower than the axle, it is stable about the pitch axis.

The only constraint here is that the entire system has to fit in the shell of the enclosing wheel.

I have adopted this configuration for the construction of the one wheel robot due to its simplicity and ease of construction.

7. Mathematics of the One Wheel Robot

Coordinate Frame Definitions

A graphical representation of the world frame and body frame axes with respect to the wheel is shown below to aid in their descriptions.

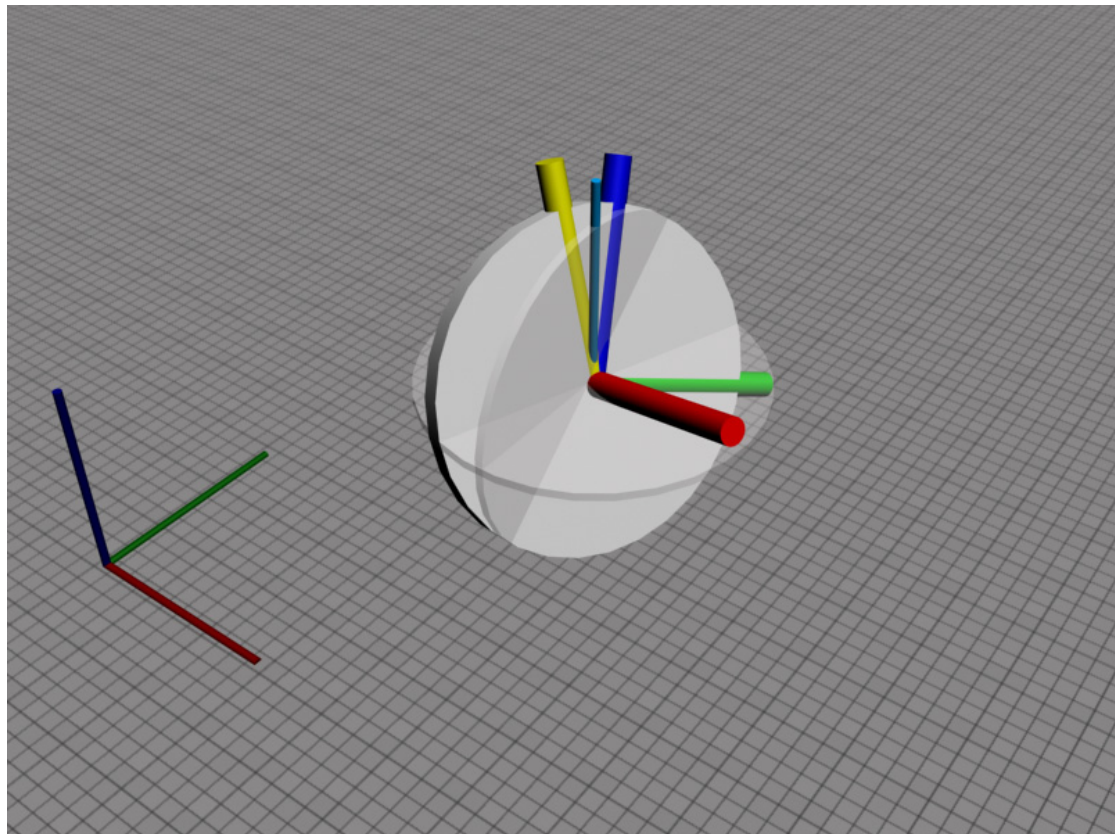


Figure 11: Axes Definitions

The world frame axes are labelled x , y , z (dark red, dark green and dark blue thin bars on the left hand of the diagram)

The body frame is labelled x' , y' , z' (bright red, bright green and bright blue thick bars attached to the white wheel)

x' axis is the axis in the body frame that is perpendicular to the disc. For zero pitch angle, the z' axis would coincide with the yellow bar.

Euler angle definitions for the system

The convention for the Euler angles used in mathematical derivations henceforth is as follows.

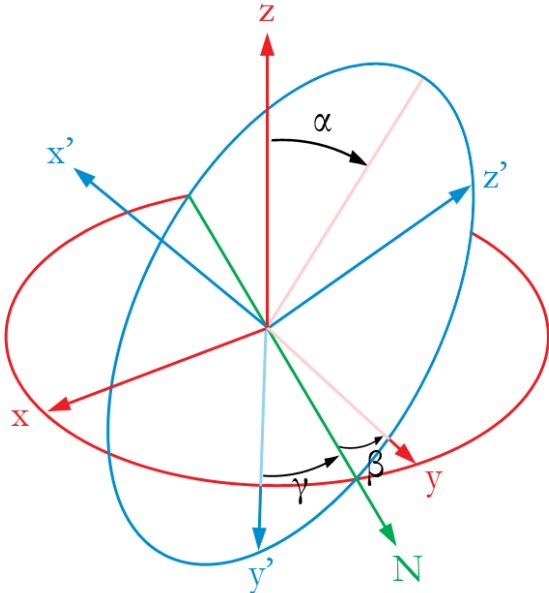


Figure 12: Euler Angles

α = The smallest angle between \vec{z} and $z'y'$ plane. This is the *roll* angle.

\vec{N} = The intersection line between $y'z'$ and xy planes. This is called the line of nodes.

β = The angle between N and y axis. This is the *yaw* angle.

γ = The angle between N and y' axis. This is the *pitch* angle.

Axis Transformations

The $\{xyz\}$ to $\{x'y'z'\}$ transformation is given by A .

$$A = R_x(\gamma)R_y(\alpha)R_z(\beta)$$

Here, R_x is the x axis rotation matrix, R_y the y axis rotation matrix, and R_z the z axis rotation matrix.

The $\{x'y'z'\}$ to $\{xyz\}$ transformation is given by $A^{-1} = A^T$.

The State Estimator

The Inertial Measurement Unit (IMU) can only measure the angular rotation rates along the x', y', and z' axes. Given these inputs, the state estimator should update the state vector at each time step.

$\omega_{x'} = \text{angular rotation about } x' \text{ axis}$

$\omega_{y'} = \text{angular rotation about } y' \text{ axis}$

$\omega_{z'} = \text{angular rotation about } z' \text{ axis}$

The Euler angular rates are given by,

$$\vec{\dot{\alpha}} = \dot{\alpha}\hat{N} = \dot{\alpha}\cos(\gamma)\hat{y}' - \dot{\alpha}\sin(\gamma)\hat{z}' \quad (13)$$

$$\vec{\dot{\beta}} = \dot{\beta}\hat{z} = \dot{\beta}\cos(\alpha)\cos(\gamma)\hat{z}' + \dot{\beta}\cos(\alpha)\sin(\gamma)\hat{y}' - \dot{\beta}\sin(\alpha)\hat{x}' \quad (14)$$

$$\vec{\dot{\gamma}} = \dot{\gamma}\hat{x}' \quad (15)$$

Resolving along the x', y' and z' axes, we get

$$\omega_{x'} = \dot{\gamma} - \dot{\beta}\sin(\alpha) \quad (16)$$

$$\omega_{y'} = \dot{\alpha}\cos(\gamma) + \dot{\beta}\cos(\alpha)\sin(\gamma) \quad (17)$$

$$\omega_{z'} = -\dot{\alpha}\sin(\gamma) + \dot{\beta}\cos(\alpha)\cos(\gamma) \quad (18)$$

These are the angular rates that will be sensed by the gyroscopes comprising the IMU. Solving these to determine the Euler angular rates,

$$\dot{\beta} = \frac{\omega_z \cos(\gamma) + \omega_y \sin(\gamma)}{\cos(\alpha)} \quad (19)$$

$$\dot{\alpha} = \omega_y \cos(\gamma) - \omega_z \sin(\gamma) \quad (20)$$

$$\dot{\gamma} = \omega_{x'} + \dot{\beta}\sin(\alpha) \quad (21)$$

Hence, at each time step, the state vector $(\dot{\alpha}, \alpha, \dot{\beta}, \beta, \dot{\gamma}, \gamma)^T$ can be computed iteratively in the following manner;

1. Compute $\dot{\beta}$ by (19)
2. Compute $\dot{\alpha}$ by (20)
3. Compute $\dot{\gamma}$ by (21)
4. Compute α by multiplying $\dot{\alpha}$ by dt
5. Compute β by multiplying $\dot{\beta}$ by dt
6. Compute γ by multiplying $\dot{\gamma}$ by dt

For small angle perturbations we can keep the linear terms and neglect higher order terms.

$$\dot{\beta} = \omega_z + \omega_y \gamma \quad (22)$$

$$\dot{\alpha} = \omega_y - \omega_z \gamma \quad (23)$$

$$\dot{\gamma} = \omega_{x'} \quad (24)$$

Hence, the state estimator update can be written as

$$\begin{bmatrix} \dot{\alpha} \\ \alpha \\ \dot{\beta} \\ \beta \\ \dot{\gamma} \\ \gamma \end{bmatrix} = \begin{bmatrix} 0 & 0 & 0 & 0 & 0 & -\omega_{z'} \\ dt & 0 & 0 & 0 & 0 & 0 \\ 0 & 0 & 0 & 0 & 0 & \omega_{y'} \\ 0 & 0 & dt & 0 & 0 & 0 \\ 0 & 0 & 0 & 0 & 0 & 0 \\ 0 & 0 & 0 & 0 & dt & 0 \end{bmatrix} \begin{bmatrix} \dot{\alpha} \\ \alpha \\ \dot{\beta} \\ \beta \\ \dot{\gamma} \\ \gamma \end{bmatrix} + \begin{bmatrix} 0 & 1 & 0 \\ 0 & 0 & 0 \\ 0 & 0 & 1 \\ 0 & 0 & 0 \\ 1 & 0 & 0 \\ 0 & 0 & 0 \end{bmatrix} \begin{bmatrix} \omega_{x'} \\ \omega_{y'} \\ \omega_{z'} \end{bmatrix} \quad (25)$$

In standard notation, equation (25) would be written as

$$x_k = A_k x_{k-1} + B u_{k-1} + w_{k-1} \quad (26)$$

Where x_k is the k^{th} estimate of the state, A_k is the state transition matrix, B the control input matrix and w the process noise.

$$x = \begin{bmatrix} \dot{\alpha} \\ \alpha \\ \dot{\beta} \\ \beta \\ \dot{\gamma} \\ \gamma \end{bmatrix}, A = \begin{bmatrix} 0 & 0 & 0 & 0 & 0 & -\omega_{z'} \\ dt & 0 & 0 & 0 & 0 & 0 \\ 0 & 0 & 0 & 0 & 0 & \omega_{y'} \\ 0 & 0 & dt & 0 & 0 & 0 \\ 0 & 0 & 0 & 0 & 0 & 0 \\ 0 & 0 & 0 & 0 & dt & 0 \end{bmatrix}, B = \begin{bmatrix} 0 & 1 & 0 \\ 0 & 0 & 0 \\ 0 & 0 & 1 \\ 0 & 0 & 0 \\ 1 & 0 & 0 \\ 0 & 0 & 0 \end{bmatrix}, u = \begin{bmatrix} \omega_{x'} \\ \omega_{y'} \\ \omega_{z'} \end{bmatrix}$$

8. Component Selection

Several crucial components had to be selected for the design of the one wheel robot. In this section, I discuss the selection process for these parts.

Reaction wheel, reaction wheel motor

From the simulations of the inverted wheel pendulum, if the weight of the entire robot is less than 4kg, then a 1kg, 6cm radius reaction wheel would be sufficient to balance the robot.

For an initial offset of 24 degrees, the initial torque required would be 2 Nm. The two possible motors from MicroMo that could be used here are micromotor 3257 and micromotor 3863. Micromotor 3257 is an 80W motor with a stall torque of 537mNm, while micromotor 3863 is a 220W motor with a stall torque of 1250mNm. The 3863 is 160g heavier and 10mm longer than the 3257, and for this application, less than 30% of its total power would be used.

For the 3257, gearbox 38/1 could be used with either a reduction of 3.7 or 14. The gearbox of reduction 3.7 would produce a maximum torque of 1.99Nm at stall. However, the stall current is 14A, and that would result in the motor dissipating 319.5W of heat. The thermal resistance (rotor to ambient) = 10K/W. Thus, the increase in temperature at stall would be beyond the thermal limits of operation.

If the reduction of 14 is used, for an output torque of 2Nm, the motor would draw 3.9A of current, which would be fine for short periods of time, as is required by this application.

For each motor selection, the nominal voltage could be chosen to be either 12V or 24V. However, for the same power output, the 12V motor would draw twice as much current as the 24V motor. This would mean that the batteries should be twice the capacity, since their maximum discharge rates are rated in terms of their capacity (20C for RC aircraft grade Lithium Polymer cells).

Hence, the selected motor and gearbox is the MicroMo 3257 (24V) with planetary gearbox 38/1, reduction 14.

Drive motor

For a total mass of 5kg (worst case scenario), wheel diameter of 32cm, desired acceleration of 2m/s^2 and maximum speed of 4m/s, the driving motor should be capable of producing 40W of power. It turns out that the same motor and gearbox combination as the reaction wheel can be used here. Using the parameters of this combination, with a constant acceleration of 2 m/s^2 , the maximum attainable speed with this acceleration is 3.89m/s. The current drawn by the motor in this case is 3.12A. For a constant acceleration of 1 m/s^2 , the maximum attainable speed with this acceleration is 4.42m/s. The current drawn by the motor in this case is 1.56A.

Batteries

For the chosen motors, the maximum current requirement is 8A. If 20C Lithium Polymer cells are chosen, then the minimum capacity of the cells should be 400mAh. However, this would give a run time of only 3 minutes. Using 2200mAh cells would give a worst case runtime of 17 minutes. This would be the case if the motors were constantly accelerating at their maximum calculated values. In reality, there will be equal times of acceleration and deceleration. While decelerating, the motors would regenerate some part of the energy by charging the batteries through the freewheeling diodes in the H-bridges. Therefore, six 2200mAh lithium polymer cells in series would suffice for the drive motors.

To electrically isolate the motor driving circuit and the control and sensors, a separate battery pack is used to supply power to the control electronics. The microcontroller draws 100mA of current, and the gyroscopes 40mA each. The accelerometers draw about 100mA of

current combined. The wireless link module draws 215mA of current. Therefore, the control electronics would require a total of 535mA of current. A lithium polymer pack of two 600mAh cells in series would suffice, and would last for more than an hour.

9. Inertial Measurement Unit Filtering

Under the small angle approximation (eq. 22-24), it turns out that each angle can be filtered and updated independently. Ideally, if we could determine the initial orientation, the orientation at any later instant of time could be obtained by the integration (summation) of the readings from the gyroscopes. Unfortunately, the readings from the gyroscope suffer from biasing errors which becomes pronounced as the readings are integrated over time. While this error is negligible for the angular rate measurements, it isn't so for angular measurements. On the other hand, if we were to take the readings from the inclinometers alone for the x and y axes, for low angular rates, the measurements would be very accurate, but at higher angular rates, and in the presence of additional accelerations, the readings from the inclinometers would be quite noisy.

Presented below are the histogram plots of the measured angular rates from the three gyroscopes while the IMU is held stationary. To draw the histograms, 4408 samples were taken over a period of 10 minutes. 1 LSB = $0.07326^\circ/\text{s}$.

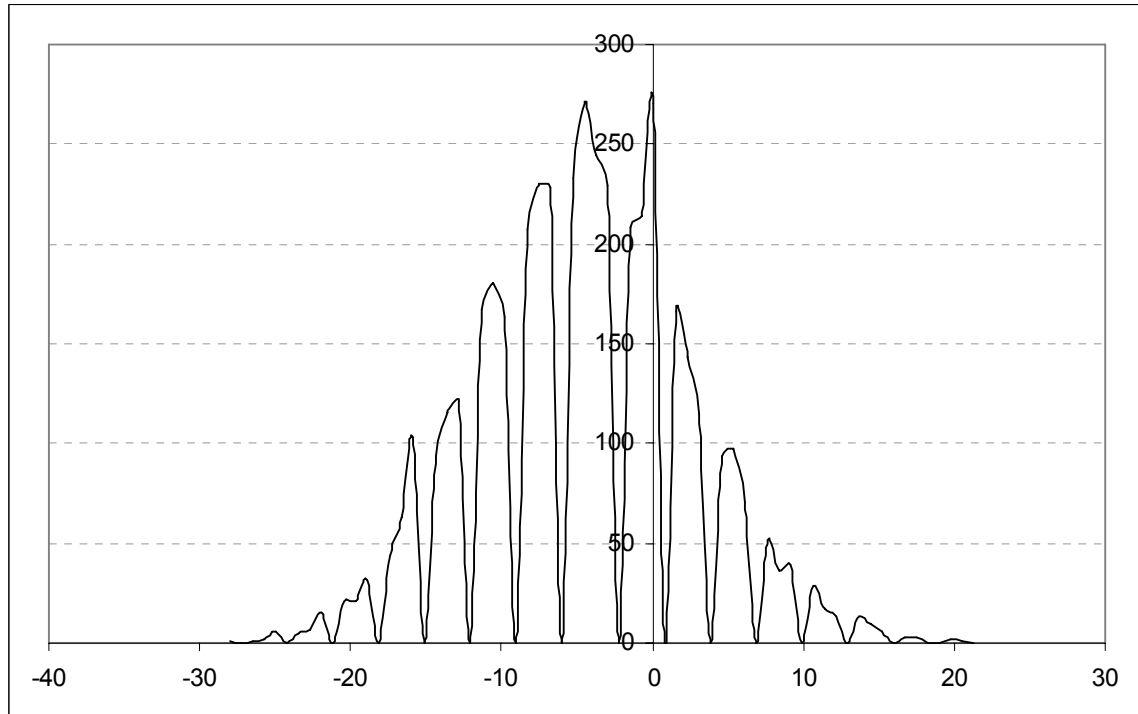


Figure 13: Histogram of readings taken from X-Axis Gyroscope

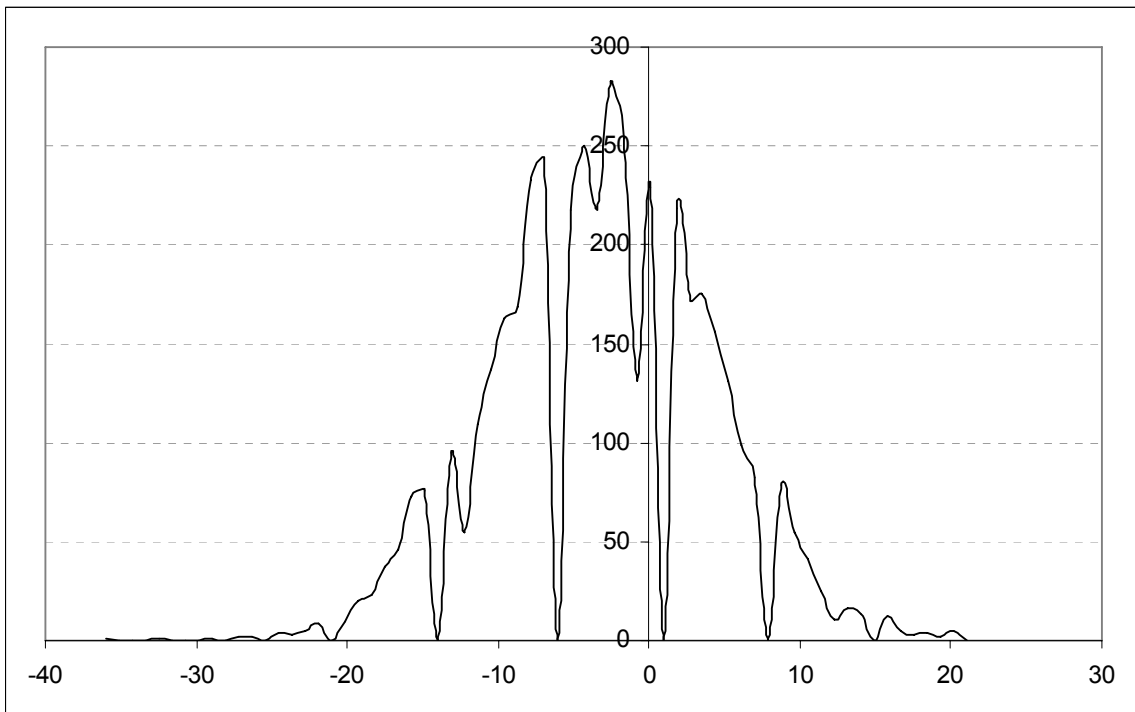


Figure 14: Histogram of readings taken from Y-Axis Gyroscope

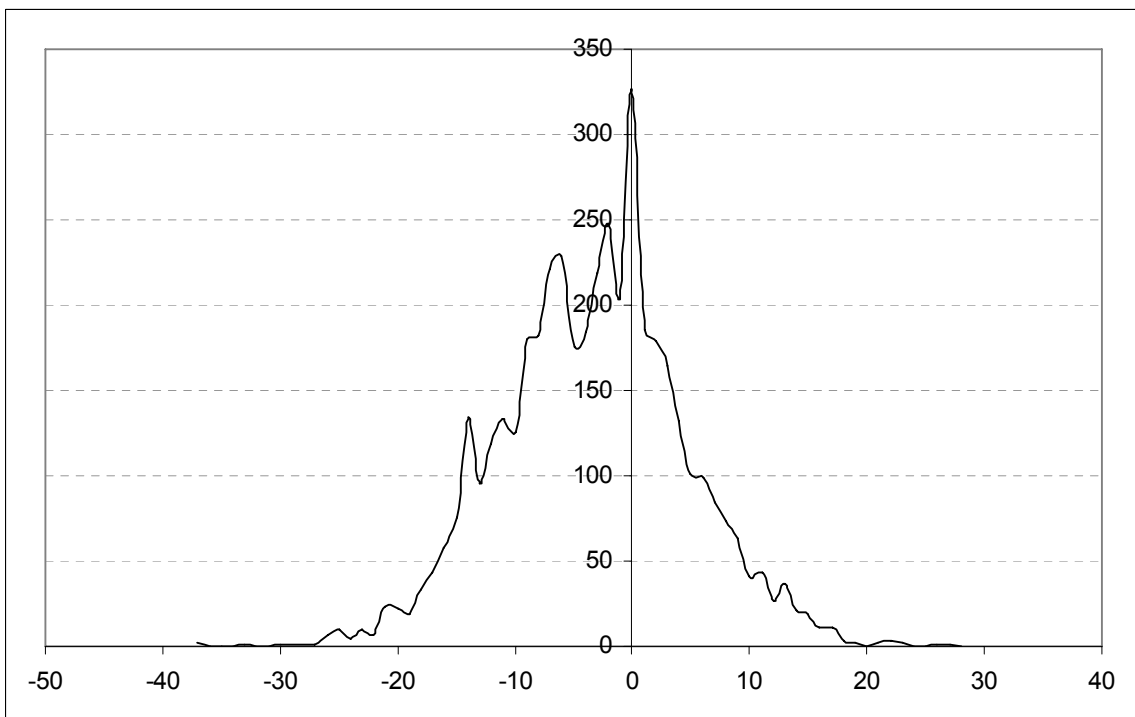


Figure 15: Histogram of readings taken from Z-Axis Gyroscope

As can be seen from the histograms, the readings do not have a zero mean, although the variation is roughly Gaussian in nature.

The angle reading from the X-Axis gyroscope, as obtained by simple summation of the readings, is plotted to show the accumulation in error. The x-axis shows the reading number, and the y-axis shows the integrated angle reading in units of 0.00997° . The last reading indicates an angle of 220.5° .

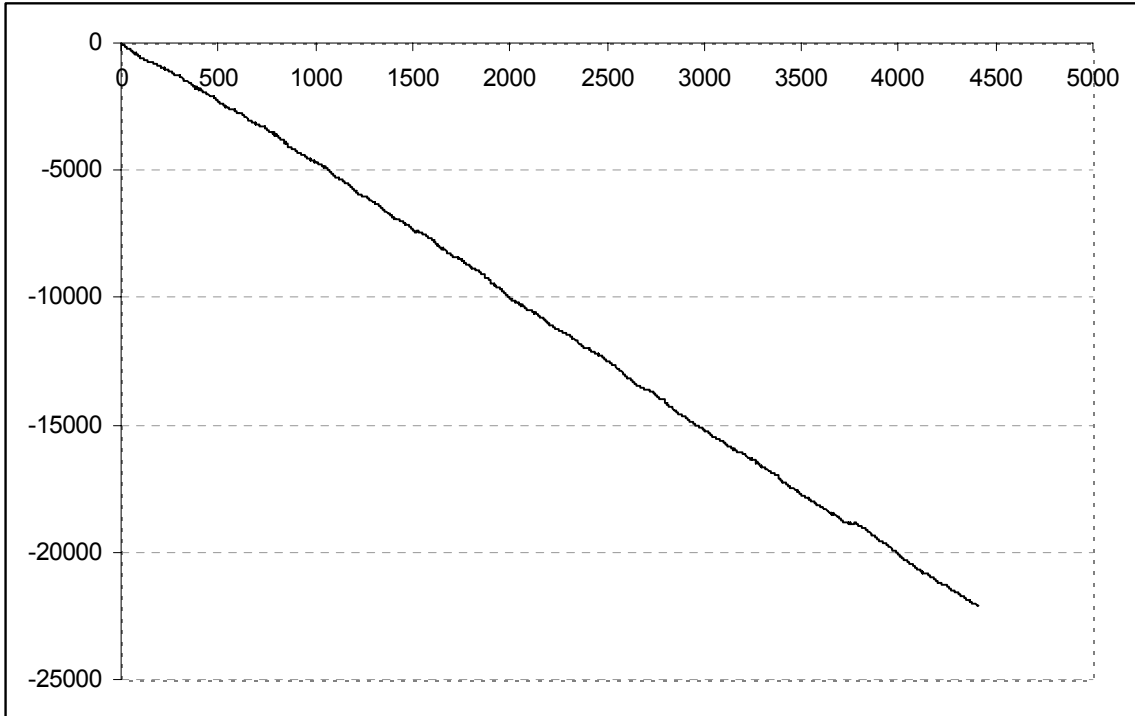


Figure 16: Variation in X-angle vs. time

One solution to the problem is to implement a complementary filter for the x and y axes. The goal is to utilise readings from both the inclinometer as well as the gyroscope in such a way that the low angular rate readings are heavily dependent on the inclinometer, while for high angular rates, the gyroscope readings play a more important role. The z axis could in principle be similarly stabilised using inputs from a magnetometer, but in this application, the absolute z axis angle is not important, and hence not further stabilised. The state equation to implement this is:

$$sY = G + b(A - \frac{Y}{1 + \tau.s})$$

Where Y is the angle, G the gyroscope rate input, and A the inclinometer (accelerometer) input. τ denotes the lowpass constant. For step inputs for both the gyroscope and accelerometer, the response is given by

$$Y = \frac{(g + a.b)(1 + \tau.s)}{s(\tau.s^2 + s + b)}$$

On the target board, the filter runs at a frequency of 2 KHz, and the lowpass of the angle is implemented using $\tau = 0.4995$

Physically, a step response with respect to G corresponds to a constant bias of $1^\circ/\text{s}$, and a step response with respect to A corresponds to a static inclination of 1° .

This filter was simulated using Matlab and Simulink, and the values for b and τ determined for critical damping. In practice, it was seen that the response was faster with a slightly underdamped system.

Presented below are some simulated and experimental results for the proposed complimentary filter.

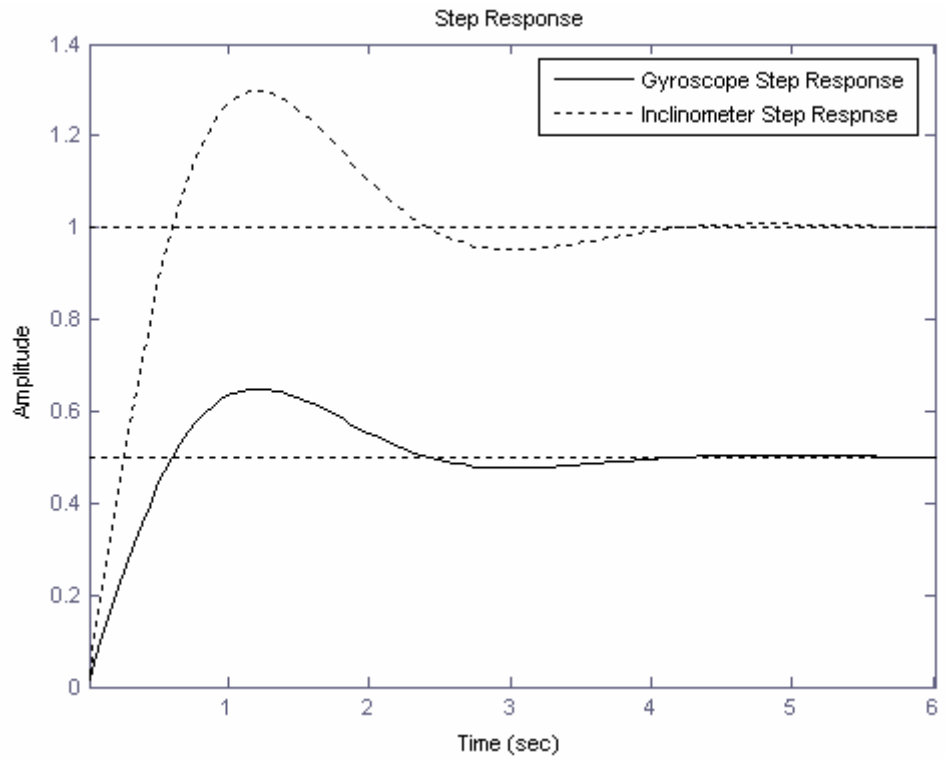


Figure 17: Simulation, b=2

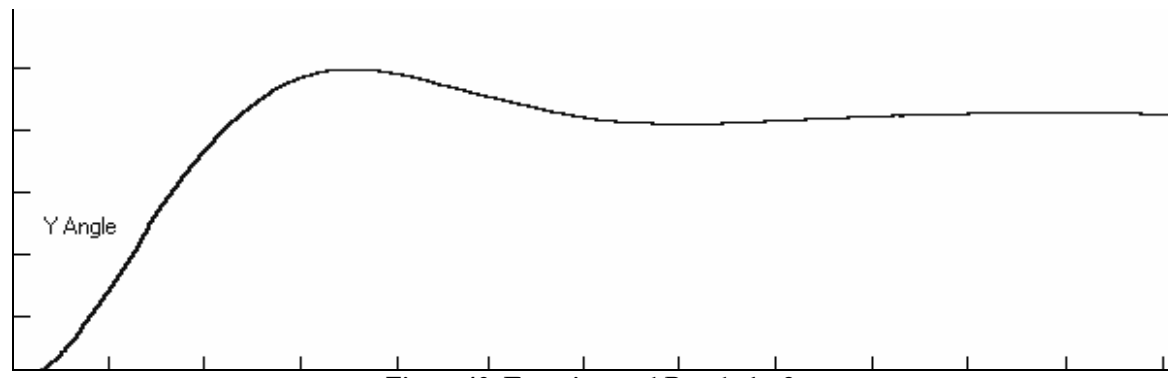


Figure 18: Experimental Result, b=2

Y-axis: 1 Unit = 3.2° , X-axis: 1 Unit = 0.5s

The experimental result is from the target board when started up at an angle of 13.7°

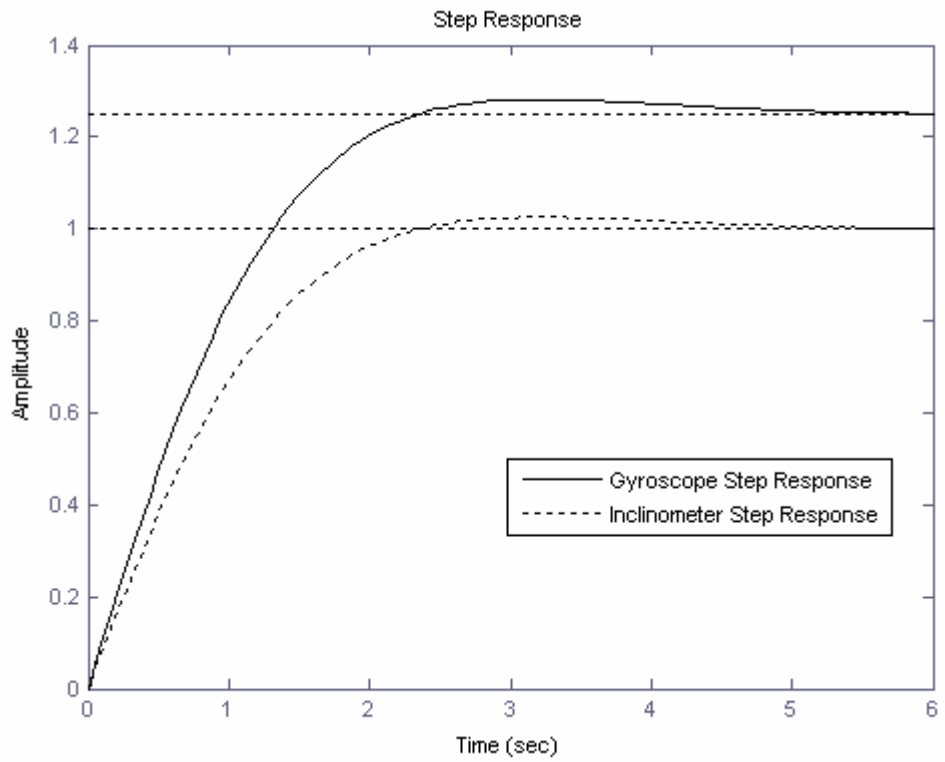


Figure 19: Simulation, $b=0.8$

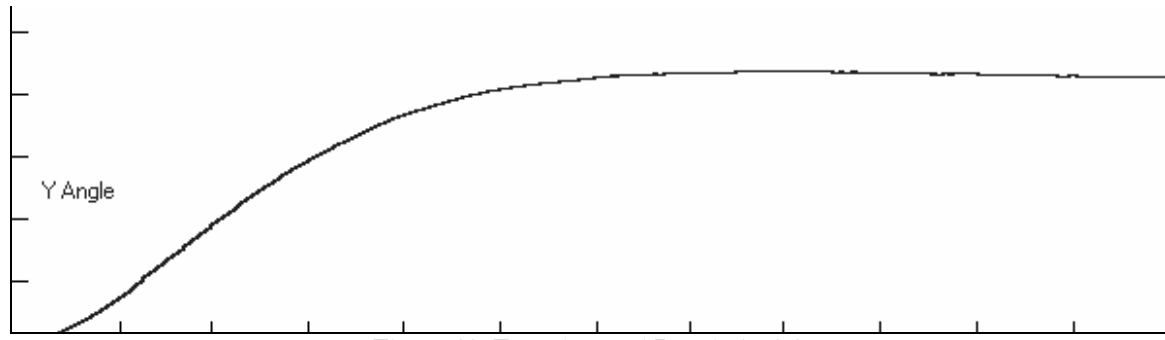


Figure 20: Experimental Result, $b=0.8$

Y-axis: 1 Unit = 3.2° , X-axis: 1 Unit = $0.5s$

The experimental result is from the target board when started up at an angle of 13.7°

It was calculated that for critical damping $b = 0.5005$.

The simulated Gyroscope step response shows a steady state error of 1.25° for a bias error of $1^\circ/s$. Actually, the maximum bias error is seen to be $0.42^\circ/s$, so this would lead to a maximum steady state error of 0.525° .

10. Mechanical Construction

To save space, and also to maintain a low centre of gravity, the drive motor is kept at an angle, and connected to the drive shaft by a pair of bevel gears. The internal structure linking the two motors, and supporting the pendulum mass is made of aluminum L-sections interlinked by dowel pins for accurate positioning of the links.

A complete CAD model of the One Wheel Robot was designed in AutoCAD to aid in the design layout and fabrication. Some of the rendered views of the robot are presented below.

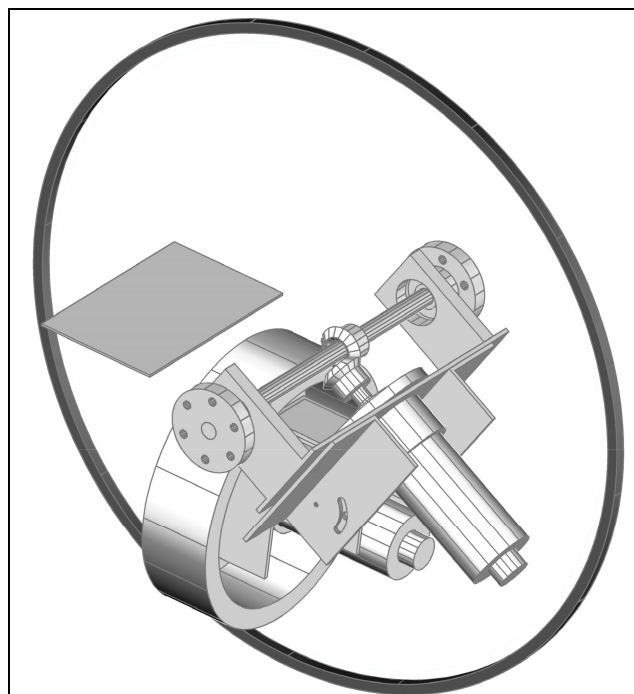


Figure 21: Perspective View

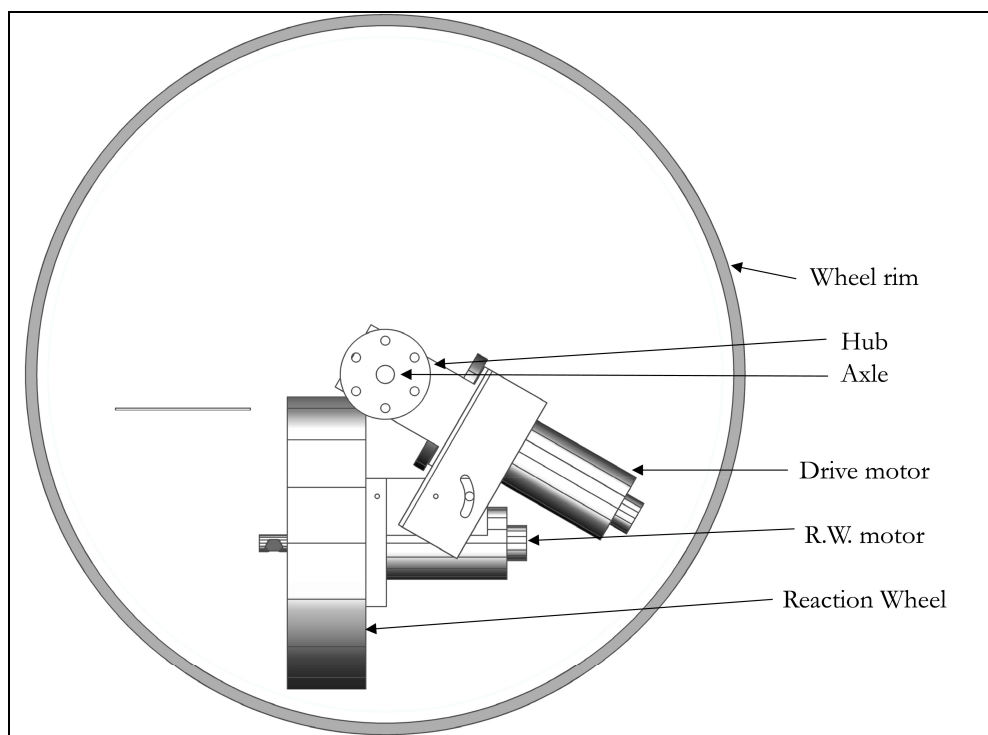


Figure 22: Side View

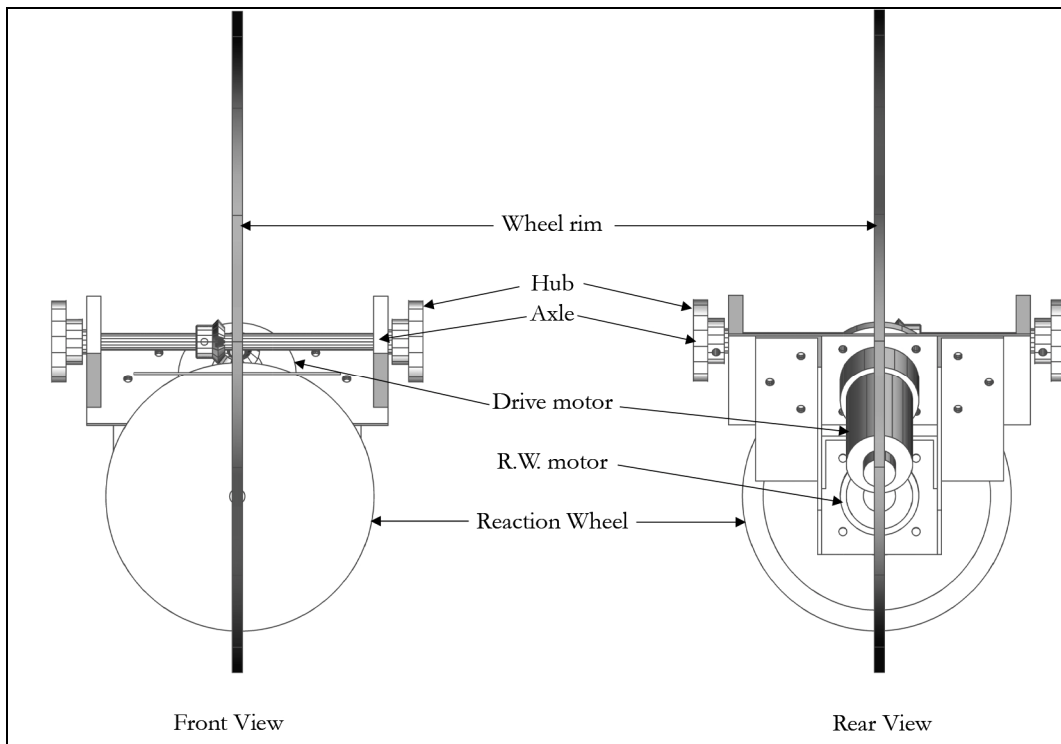


Figure 23: Front and Rear Views

11. Test Rig

In order to test the balancing of the system, and to tune it before incorporating it into the enclosed wheel, a test rig was constructed that is used to suspend the structure and constrain its motion to rotation about the roll axis. This was done in a manner to best mimic the effect of suspending the system from the axle of the enclosed wheel.

All the tests with the control system for balancing the system were conducted on this test rig. A rendered view of the CAD model of the test rig is shown below, along with a photograph of the actual setup.

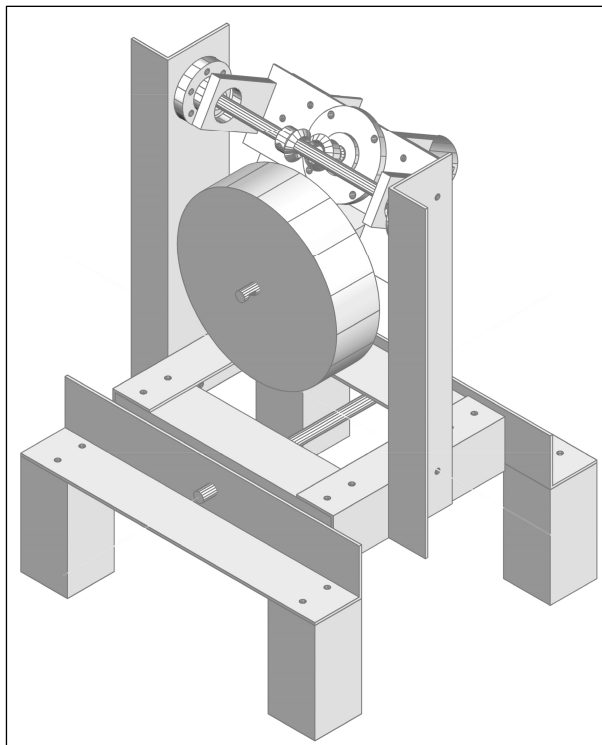


Figure 24: CAD Rendering of Test Rig

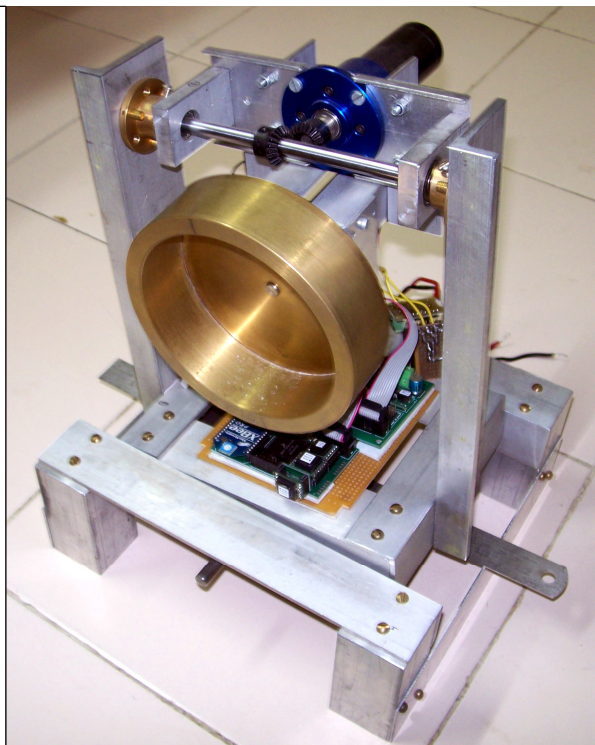


Figure 25: Actual Test Rig

12. Electronics

There are three major sub-systems in the electronics design, the IMU, the microcontroller and wireless link, and the Motor drivers.

In addition to this, for the RF link ground station, a USB Zigbee module was developed which could be connected to the PC for telemetry and control.

The Inertial Measurement Unit (IMU)

The IMU is comprised of three MEMS gyroscopes (Analog Devices ADIS16250 programmable SPI interface gyroscope) and two MEMS inclinometers (Analog Devices ADIS16201 programmable SPI interface dual axis accelerometer / inclinometer).

The ADIS16250's are digital out gyroscopes with an SPI interface. They require a 5V supply for the onboard charge pump which generates 15V for the MEMS vibrator. The digital interface, however, is 3.3V.

The ADIS16201's are digital out dual axis accelerometer/inclinometers with an SPI interface. They require only a 3.3V supply, and their digital interface is 3.3V. They compute the inclination angle internally assuming the inclinometer to be mounted perfectly along the vertical plane. The raw accelerometer readings are also accessible.

To reduce the effect of electrical noise on the sensors, a separate low dropout, low noise regulator, REG104-5 is used to regulate the 5V supply for the gyroscopes, and REG104-3.3 to regulate the 3.3V supply for the accelerometers.

The microcontroller and wireless link

The microcontroller used here is the ARM7 based Freescale MAC7121. This microcontroller has a host of peripherals which are useful in this application- the SPI port, multiple serial ports, and a powerful eMIOS (Enhanced Modular I/O Subsystem). The eMIOS ports can be configured for output pulse width and frequency modulation, hardware quadrature decoding, and a host of other modes. In this application, the eMIOS port is used to provide the PWM signals to the motor drivers, and also to decode the output from the encoders. The ARM7 core runs at 50MHz, at a maximum execution speed of 50MIPS. The 32bit ARM7 core, along with 512Kb of flash, 32Kb of data flash, and 32Kb of SRAM provides ample computing power.

The wireless link is implemented using a Zigbee Pro (XBee-PRO™ OEM) module. This module works in the ISM band with a carrier frequency of 2.4GHz. Its indoor range is rated at 100m, and has a maximum data rate of 115.2Kbps. This wireless link would be used for telemetry and to issue control signals to the robot.

The Motor Drivers

The H-bridges driving the motors must be capable of providing up to 10A of continuous current and switching at 24 KHz. I designed my own H-bridges for this purpose using TI's ucc27201 high side/low side N-channel MOSFET drivers. The MOSFET's used are STD95NH02L, which has a maximum rated drain current of 80A, and a drain resistance (on) of $5\text{m}\Omega$ at a gate voltage of 10V. Hence, with a drain current of 10A, the power dissipation per MOSFET would be only 0.5W. These MOSFET's have a DPAK package, so the drain metal tab is soldered directly to the PCB, and helps in dissipating heat away from the die. To aid in the thermal dissipation, the drain metal tab of the MOSFET's are directly soldered onto 10mm x 15mm copper planes, in accordance with AN994, International Rectifier[4]. This should theoretically provide a thermal dissipation of 4.5W per MOSFET.

The USB Zigbee module

The USB Zigbee module is based on the TUSB3410 USB to serial port controller. When connected to the PC, the module shows up as an additional COM port. The serial interface of the Zigbee module is directly connected to the serial interface of the TUSB3410. The telemetry ground station software that was developed in VB can be used to communicate with the target system using this module.

The circuit boards were designed in Eagle PCB Layout editor. The layouts for the boards shown below are drawn to scale.

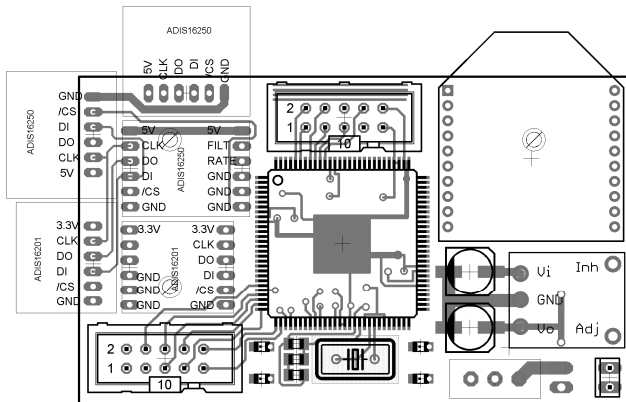


Figure 26: Main Board, Top side

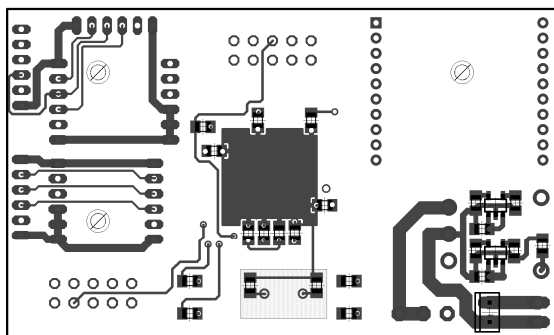


Figure 27: Main Board, Bottom side

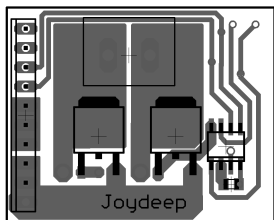


Figure 28: H-bridge Module, Top side

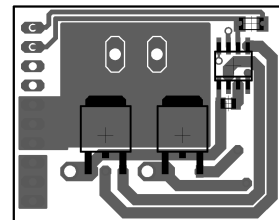


Figure 29 H-bridge Module, Bottom side

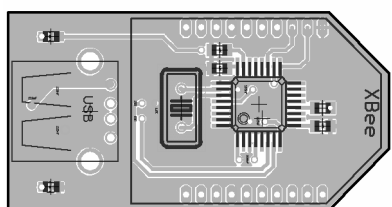


Figure 30: USB Zigbee Module, Top side

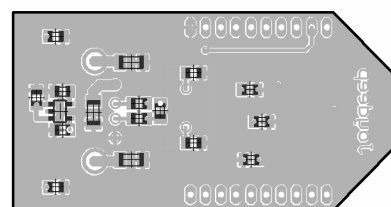


Figure 31: USB Zigbee Module, Bottom side

13. Telemetry and Control

To help aid in the tuning of the system, and to collect data from the system, a telemetry station software was written in Visual Basic. This could then be used with the USB Zigbee module to setup a wireless link with the one wheel robot for telemetry and control. The telemetry software is capable of graphically displaying the time variation of up to six channels, and saving the graphs to bitmap files. Alternatively, a plaintext listing of the values can be saved for analysis with other software like Excel. This was indispensable while developing the IMU complimentary filters and while tuning the control loop.

A screenshot of the telemetry station is shown below.

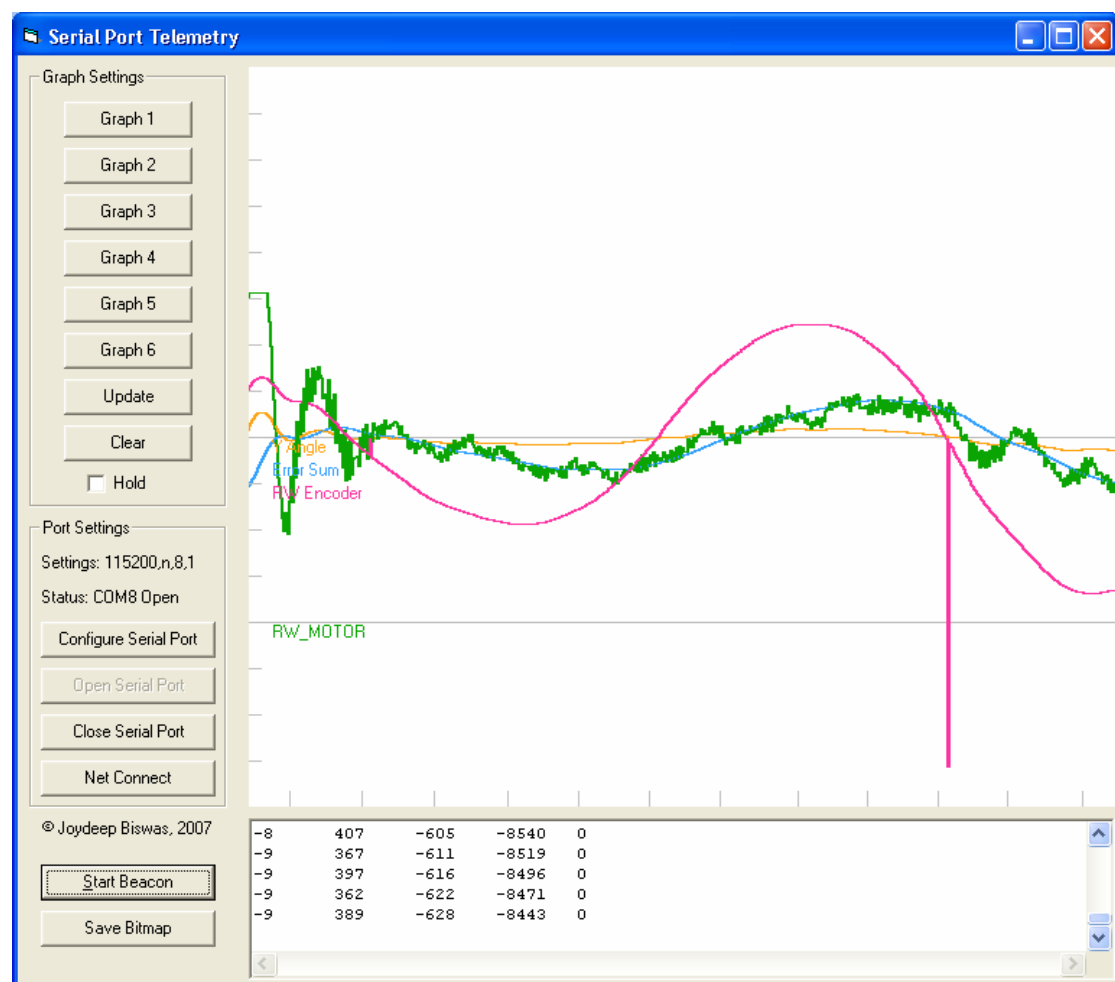
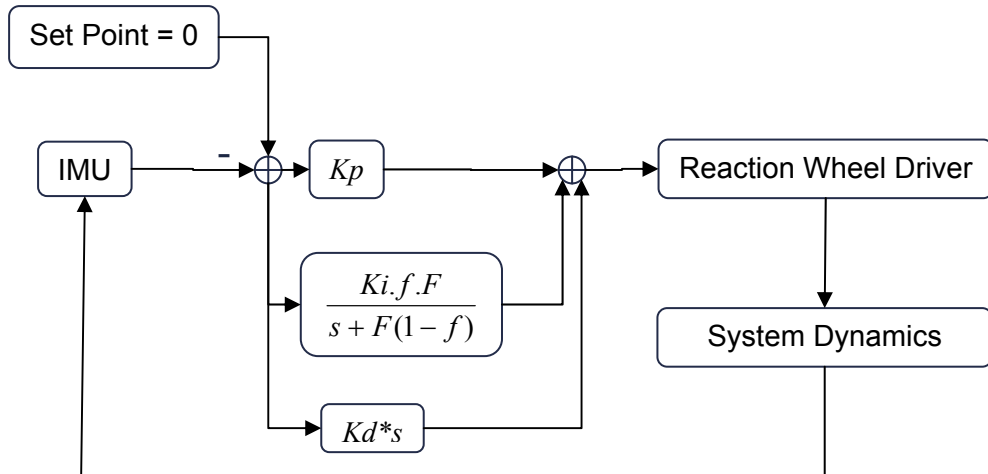


Figure 32: Ground Station Telemetry Software

14. Control System

The single wheel robot incorporates feedback from the IMU as well as the reaction wheel encoder to estimate the offset from the equilibrium position and the equilibrium point of the system.

As a first step, a PID-like loop was implemented by taking feedback from the IMU alone. Here, it was assumed that the system is symmetric, so the equilibrium position would be the vertical position.



For the test run, $K_p = 40$, $K_i = 0.1$, $K_d = 1.0$, $f=0.99$, $F = \text{Control Loop Update frequency, 2KHz}$

The integrated error is limited to a maximum of $\text{ErrorSum} = 100000$ and is set to decay exponentially with a time constant of approximately 1.5s (determined by f). The decay helps in nullifying the effect of errors that occurred much earlier. Without this decay, it is seen that the system becomes unstable if the initial (startup) position is far from the equilibrium position.

The experimental result of this test is shown below, as captured by the telemetry station:

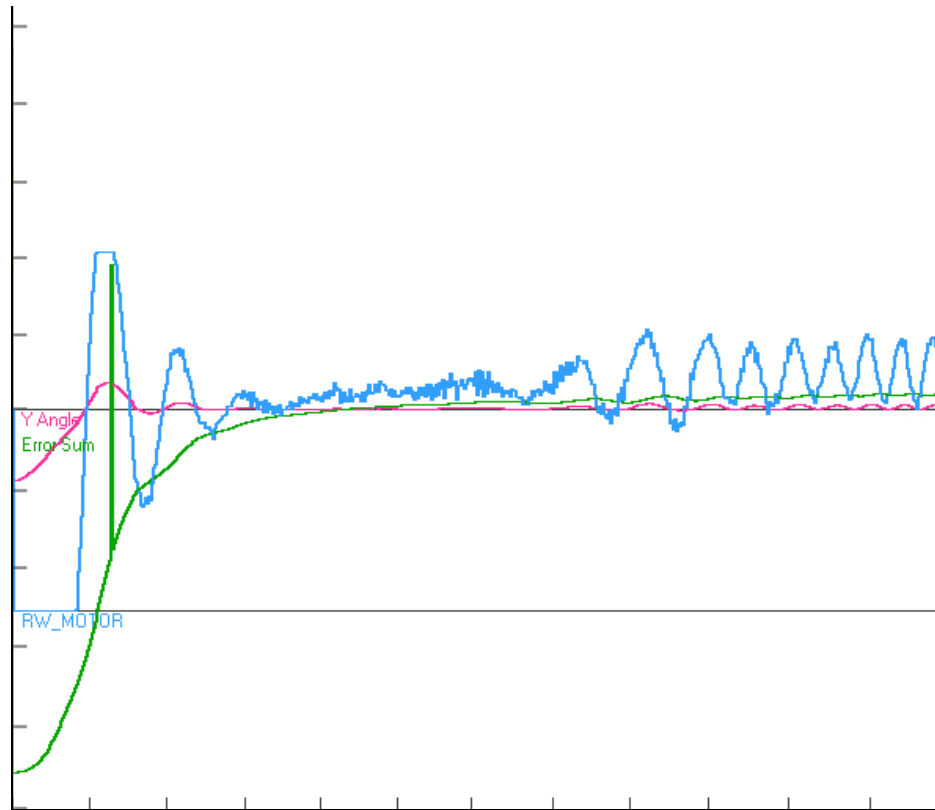
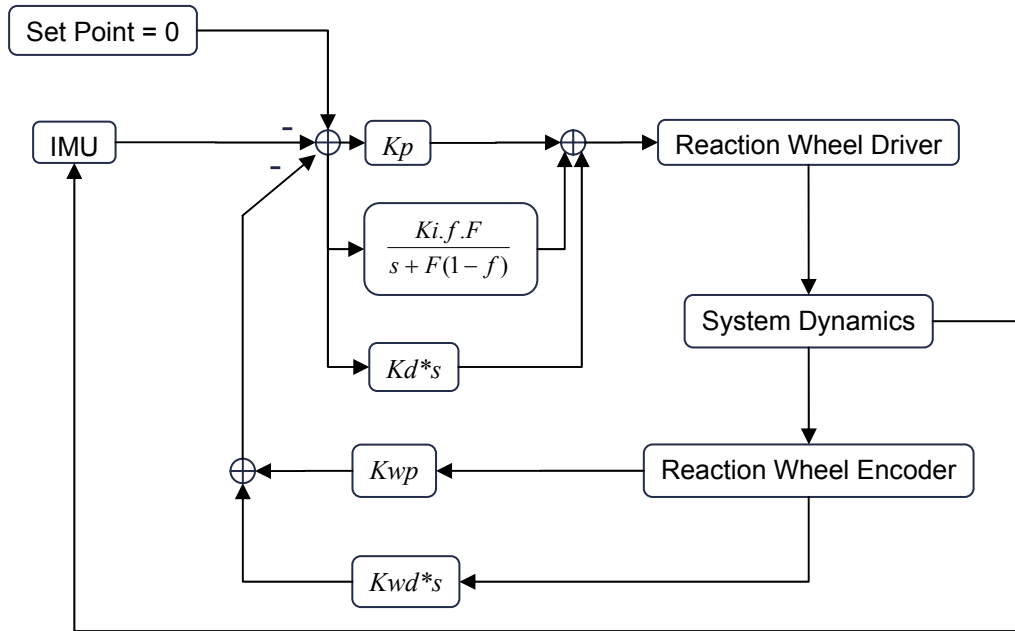


Figure 33: Y Angle, Error Sum, RW Motor Out vs. time

Y-Axis:
RW_Motor (Blue): Reaction Wheel Motor 10bit PWM, 1 unit = 256
Error Sum (Green): Integral of error with decay, 1 unit = 0.5° s
Y Angle (Pink): Tilt angle, 1 unit = 5 degrees
X-Axis: 1 unit = 0.5s

From the test run, it was seen that the system is able to recover from the initial offset of 5 degrees, but as time passes, the error in the estimated equilibrium position causes the reaction wheel to “run away”, making the system unstable. The oscillatory nature of the Y angle (after 4s) is because the reaction wheel is not perfectly symmetric and hence it makes the system wobble a bit.

The second step was to incorporate feedback from the reaction wheel encoder to dynamically estimate the equilibrium position of the system.



For the test run, $K_p = 40$, $K_i = 0.1$, $K_d = 1.0$, $K_{wp} = 0.0009$, $K_{wd} = 0.00001$, $f=0.99$, $F =$ Control Loop Update frequency, 2KHz

The encoder provides $4*512*3.7$ counts per rotation of the reaction wheel, which corresponds to 21 counts per degree.

The experimental result of this test is shown below, as captured by the telemetry station:

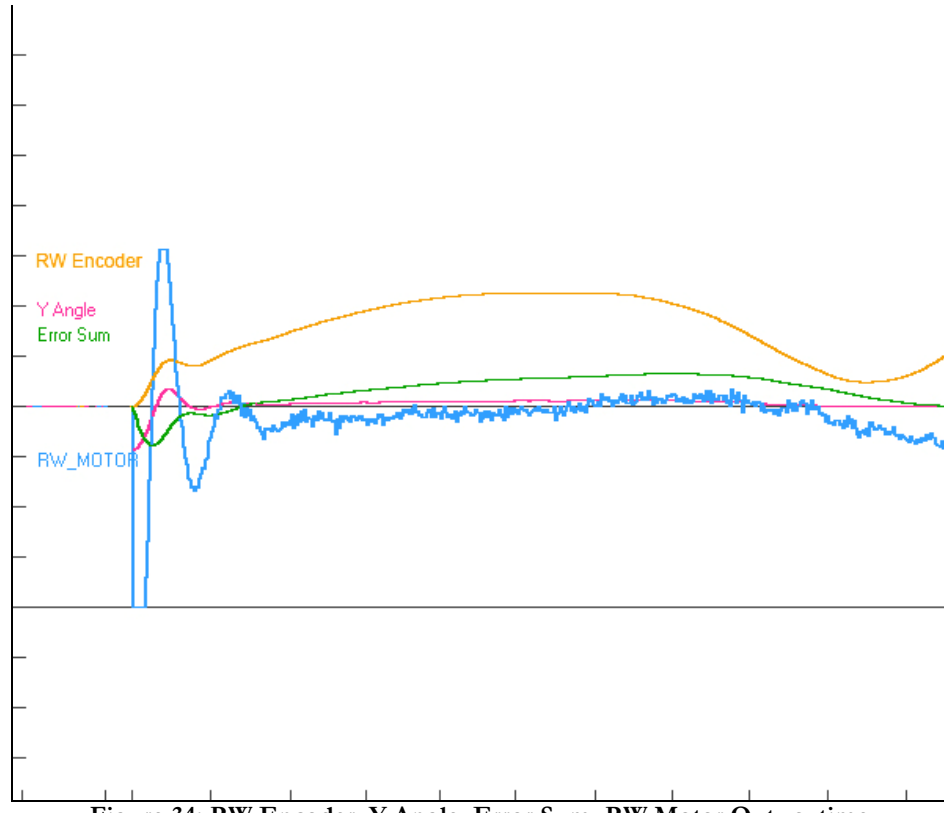


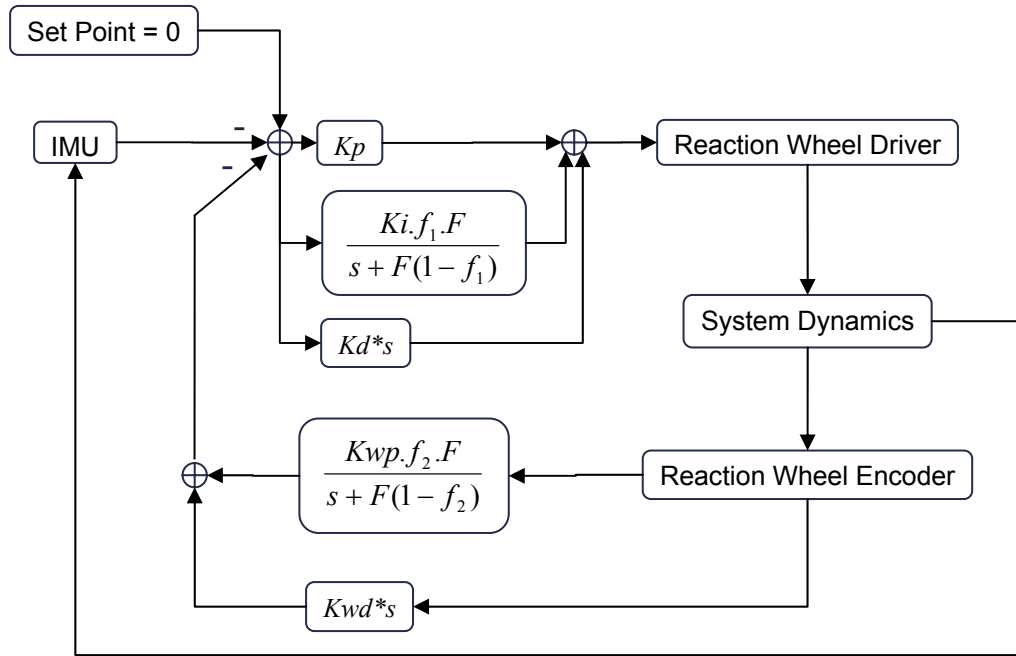
Figure 34: RW Encoder, Y Angle, Error Sum, RW Motor Out vs. time

Y-Axis:
RW_Motor (Blue): Reaction Wheel Motor 10bit PWM, 1 unit = 128
Error Sum (Green): Integral of error with decay, 1 unit = 0.32°s
Y Angle (Pink): Tilt angle, 1 unit = 3.2 degrees
RW Encoder (Orange): Reaction Wheel Encoder, 1 unit = 121°

X-Axis: 1 unit = 0.5s

The system is much more stable now, and the steady state value of Y Angle corresponds to the dynamic estimate of the system equilibrium position. However, if the system is started up at a large offset from the equilibrium position, the error in the RW Encoder accumulates as the RW is spun up to regain balance. This leads to an oscillatory motion, as is seen in the above plot, where (4s after start-up) the RW motor starts spinning in the opposite direction as the beginning of the oscillatory motion.

One solution to the oscillation problem due to accumulation of initial RW Encoder values, is to decay the RW Encoder readings too, as was done with the Error Sum.



For the test run, $K_p = 40$, $K_i = 0.1$, $K_d = 1.0$, $K_{wp} = 0.0009$, $K_{wd} = 0.00001$, $f_1 = 0.99$, $f_2 = 0.9995$, $F = \text{Control Loop Update frequency, 2KHz}$

The experimental result of this test is shown below, as captured by the telemetry station:

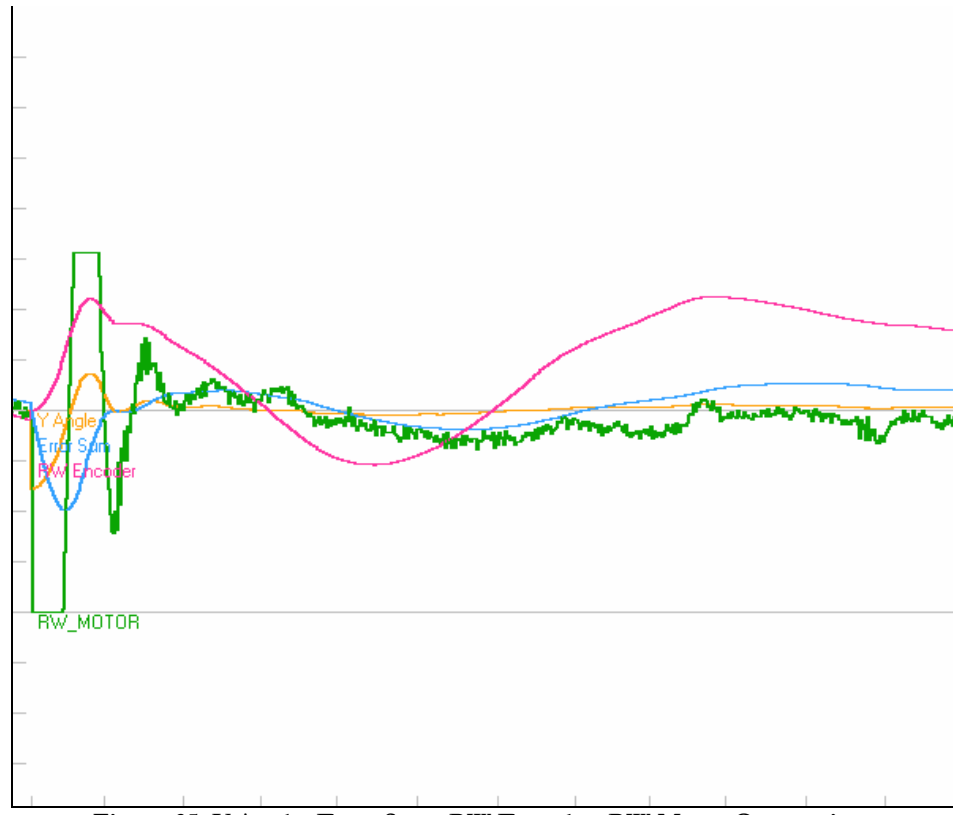
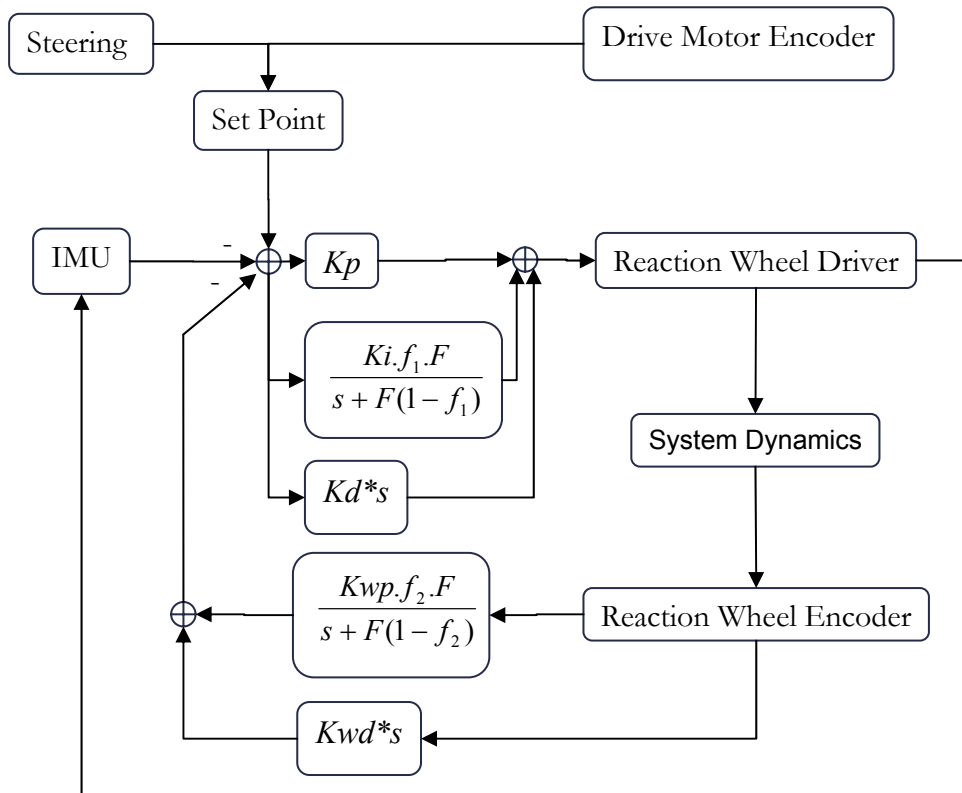


Figure 35: Y Angle, Error Sum, RW Encoder, RW Motor Out vs. time

- Y-Axis:
Y Angle (Orange): Tilt angle, 1 unit = 3.2 degrees
Error Sum (Blue): Integral of error with decay, 1 unit = 0.32°·s
RW Encoder (Pink): Reaction Wheel Encoder, 1 unit = 121°
RW_Motor (Green): Reaction Wheel Motor 10bit PWM, 1 unit = 128
- X-Axis: 1 unit = 0.5s

This system is seen to be very stable. It was experimentally seen to be stable over time and resilient to external perturbations and changes in the mass distribution of the system.

Once the system is integrated into the single wheel, the set point won't be set to zero, but rather varied according to the steering input and the current linear velocity, as measured by the main drive encoder.



15. Conclusion and Outlook

I believe the main aim of this project, to design a single wheel robot is largely complete, although due to delays in the mechanical fabrication, the complete system could not be integrated in time.

The actual project started out with the selection of the configuration of the single wheel robot. Once the enclosed wheel configuration was chosen, some time was spent on mathematically analysing the dynamics of the system, and initial simulations were conducted to demonstrate the feasibility of the idea. Further study was conducted to devise the Inertial Measurement Unit and State Estimator for the system. After the critical components for this application were chosen, the electronic systems and mechanical components were fabricated, along with a test rig to test the system. The wireless telemetry ground station proved invaluable during the development of the control system to balance the robot. The control system itself was built up in stages, each step being an improvement on the previous until a rugged, stable system was finally achieved.

Unfortunately, considerable time was lost during the mechanical fabrication, due to which not much time could be spared for the final system integration.

As further work, I intend to complete the integration of the enclosed wheel structure. This should be quite straightforward, since the system is already capable of balancing on its own, and is able to dynamically find its equilibrium position. At most, the control system parameters might need some fine tuning to adapt to the change in the moment of inertia of the fully assembled system.

Once this is done, a number of avenues would be open for exploration. Automated linear motion would be the first logical step, followed by automated turning. This could finally lead to autonomous path following.

16. References

- [1] <http://xkcd.com/332/>. Reproduced under the Creative Commons 2.5 license (<http://creativecommons.org/licenses/by-nc/2.5/>).
- [2] *Modem Mechanix and Inventions*. June 1935.
- [3] A. Al Mamun, Z. Zhen, P. Vadakkepat, and T.H. Lee. Tracking control of the gyrobot-a gyroscopically stabilized single-wheeled robot. In *Industrial Electronics Society, 2005. IECON 2005. 31st Annual Conference of IEEE*, pages 6 pp.–, 2005.
- [4] Application Note AN-994. *Maximizing the Effectiveness of Your SMD Assemblies*. International Rectifier Corporation, www.irf.com.
- [5] M.G. Bekker. *Theory of Land Locomotion: The Mechanics of Vehicle Mobility*. University of Michigan Press, 1956.
- [6] H.B. Jr. Brown and Yangsheng Xu. A single wheel, gyroscopically stabilized robot. *Robotics & Automation Magazine, IEEE*, 4(3):39–44, 1997.
- [7] Khac Duc Do, Zhong-Ping Jiang, and Jie Pan. A global output-feedback controller for simultaneous tracking and stabilization of unicycle-type mobile robots. *Robotics and Automation, IEEE Transactions on*, 20(3):589–594, 2004.
- [8] F. Grassler, A. D'Arrigo, S. Colombi, and A.C. Rufer. Joe: a mobile, inverted pendulum. *Industrial Electronics, IEEE Transactions on*, 49(1):107–114, 2002.
- [9] R.C Hemmings. Improvement in velocipede. US. Patent, 92,528,1869.
- [10] A. Koshiyama, H. Yoshinada, and K. Yamafuji. Development and motion control of the all-direction steering-type mobile robot. *Proc. 24th Int. Symp. on Industrial Robots*, pages 445–453, 1993.
- [11] S. Majima and T. Kasai. A controller for changing the yaw direction of an underactuated unicycle robot.
- [12] S. Mori, H. Nishihara, and K. Furuta. Control of unstable mechanical system control of pendulum. *International Journal of Control*, 23(5):673–692, 1976.
- [13] Z. Sheng and K. Yamafuji. Realization of a human riding a unicycle by a robot. In *Robotics and Automation, 1995. Proceedings., 1995 IEEE International Conference on*, volume 2, pages 1319–1326 vol.2, 1995.
- [14] M. Spong, P. Corke, and R. Lozano. Nonlinear control of the inertia wheel pendulum, 1999.
- [15] Mark W. Spong, Peter Corke, and Rogelio Lozano. Nonlinear control of the reaction wheel pendulum. *Automatica*, 37(11):1845–1851, November 2001.
- [16] D.W. Vos. Dynamics and nonlinear, adaptive control of an autonomous unicycle. 1989.
- [17] D.V. Zenkov, A.M. Bloch, and J.E. Marsden. Stabilization of the unicycle with rider. In *Decision and Control, 1999. Proceedings of the 38th IEEE Conference on*, volume 4, pages 3470–3471 vol.4, 1999.

Appendix A: Motor, Gearbox, Encoder datasheets

The reaction wheel is driven by a 24V MicroMo 3257 PMDC motor with a reduction of 3.7 using the 38/1 gearbox. The main drive motor is again a 24V MicroMo 3257 PMDC motor but with a reduction of 14.4 using the 38/1 gearbox. Both motors have integrated magnetic encoders with a resolution of 512cpr.

The relevant pages from the Faulhaber Data book are reproduced here for ready reference.

DC-Micromotors

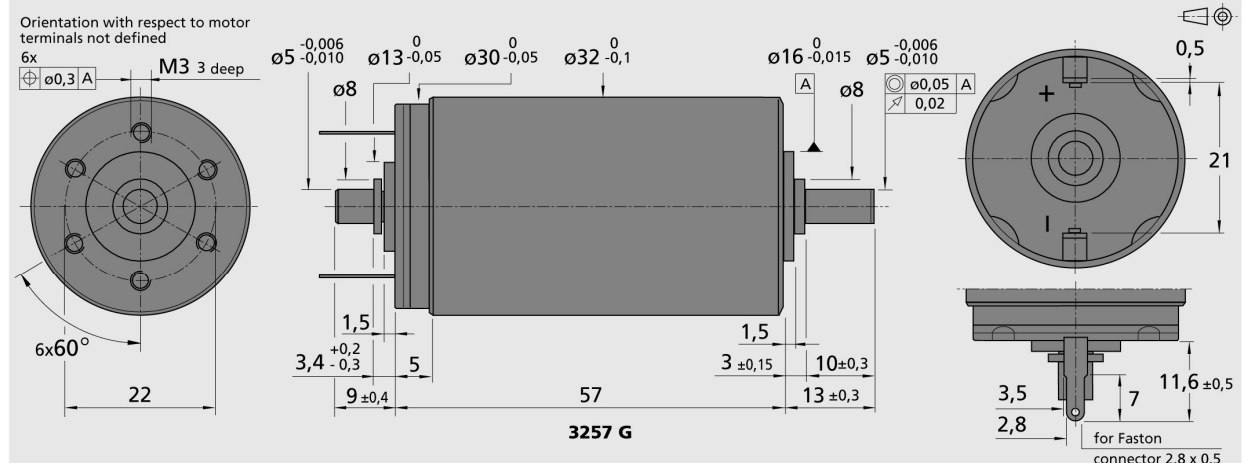
Graphite Commutation

70 mNm

For combination with (overview on page 14-15)
 Gearheads:
 32/3, 38/1, 38/2
 Encoders:
 IE2 – 16 ... 512, 5500, 5540

Series 3257 ... CR

	3257 G	012 CR	024 CR	048 CR		
1 Nominal voltage	U _N	12	24	48	Volt	
2 Terminal resistance	R	0,41	1,63	6,56	Ω	
3 Output power	P _{2 max.}	79,2	83,2	84,5	W	
4 Efficiency	η max.	83	83	83	%	
5 No-load speed	n _o	5 700	5 900	5 900	rpm	
6 No-load current (with shaft ø 5,0 mm)	I _o	0,258	0,129	0,064	A	
7 Stall torque	M _H	531	539	547	mNm	
8 Friction torque	M _F	4,9	4,9	4,9	mNm	
9 Speed constant	k _n	500	253	125	rpm/V	
10 Back-EMF constant	k _E	2,00	3,95	7,98	mV/rpm	
11 Torque constant	k _M	19,1	37,7	76,2	mNm/A	
12 Current constant	k _I	0,052	0,027	0,013	A/mNm	
13 Slope of n-M curve	Δn/ΔM	10,7	10,9	10,8	rpm/mNm	
14 Rotor inductance	L	70	270	1 100	μH	
15 Mechanical time constant	τ _m	4,7	4,7	4,7	ms	
16 Rotor inertia	J	42	41	42	gcm ²	
17 Angular acceleration	α max.	130	130	130	·10 ³ rad/s ²	
18 Thermal resistance	R _{th 1} / R _{th 2}	2 / 8			K/W	
19 Thermal time constant	τ _{w1} / τ _{w2}	17 / 810			s	
20 Operating temperature range:						
– motor		– 30 ... + 125			°C	
– rotor, max. permissible		+ 155			°C	
21 Shaft bearings		ball bearings, preloaded				
22 Shaft load max.:						
– with shaft diameter		5,0			mm	
– radial at 3 000 rpm (3 mm from bearing)		50			N	
– axial at 3 000 rpm		5			N	
– axial at standstill		50			N	
23 Shaft play:						
– radial	≤	0,015			mm	
– axial	=	0			mm	
24 Housing material		steel, black coated				
25 Weight		242			g	
26 Direction of rotation		clockwise, viewed from the front face				
Recommended values - mathematically independent of each other						
27 Speed up to	n _{e max.}		5 000	5 000	5 000	rpm
28 Torque up to	M _{e max.}		70	70	70	mNm
29 Current up to (thermal limits)	I _{e max.}		4,60	2,30	1,15	A



For details on technical information and lifetime performance refer to pages 28-34.
 Edition 2006-2007

For options on DC-Micromotors refer to page 64.
 Specifications subject to change without notice.
www.faulhaber-group.com

Planetary Gearheads

10 Nm

For combination with (overview on page 14-15)
 DC-Micromotors:
 3242, 3257, 3557, 3863
 Brushless DC-Servomotors:
 3056, 3564

Series 38/1, 38/2

	38/1 and 38/2									
Housing material	metal									
Geartrain material	steel ¹⁾									
Recommended max. input speed for:	4 000 rpm									
– continuous operation	$\leq 1^\circ$									
Backlash, at no-load	ball bearings, preloaded									
Bearings on output shaft										
Shaft load, max.:										
– radial (10 mm from mounting face)	$\leq 300 \text{ N}$									
– axial	$\leq 300 \text{ N}$									
Shaft press fit force, max.	$\leq 350 \text{ N}$									
Shaft play (on bearing output):										
– radial	$\leq 0,015 \text{ mm}$									
– axial	$\leq 0,15 \text{ mm}$									
Operating temperature range	$-20 \dots +125^\circ\text{C}$									

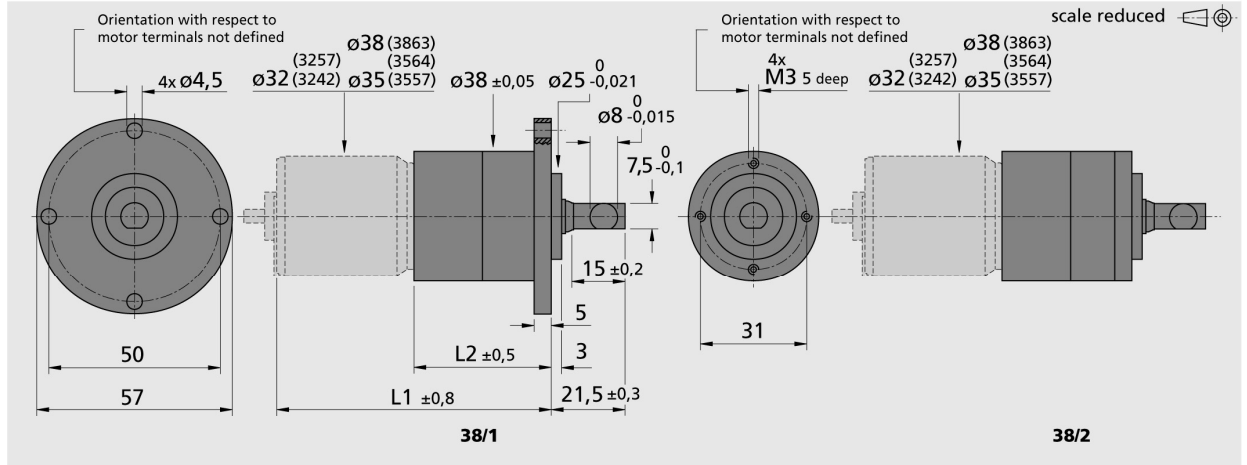
Specifications												
reduction ratio (nominal)	weight without motor ²⁾	length without motor	length without motor 3863	length with motor					output continuous operation	torque intermittent operation	direction of rotation (reversible)	efficiency
				3242 G	3056 K	3257 G	3557 K	3564 K				
3,71:1	166	32,3	27,3	74,3	88,3	89,3	96,3	91,3	6,0	8,0	=	88
14 :1	215	40,1	35,1	82,1	86,1	97,1	104,1	99,1	0,4 (10)	0,6 (15)	=	80
43 :1	268	47,9	42,9	89,9	103,9	104,9	111,9	106,9	1,4 (10)	1,9 (15)	=	70
66 :1	268	47,9	42,9	89,9	103,9	104,9	111,9	106,9	2,2 (10)	2,9 (15)	=	70
134 :1	318	55,7	50,7	97,7	111,7	112,7	119,7	114,7	4,5 (10)	6,0 (15)	=	60
159 :1	320	55,7	50,7	97,7	111,7	112,7	119,7	114,7	5,3 (10)	7,0 (15)	=	60
246 :1	320	55,7	50,7	97,7	111,7	112,7	119,7	114,7	8,2 (10)	11 (15)	=	60
415 :1	372	63,5	58,5	105,5	119,5	120,5	127,5	122,5	10 (10)	15 (15)	=	55
592 :1	372	63,5	58,5	105,5	119,5	120,5	127,5	122,5	10 (10)	15 (15)	=	55
989 :1	374	63,5	58,5	105,5	119,5	120,5	127,5	122,5	10 (10)	15 (15)	=	55
1 526 :1	378	63,5	58,5	105,5	119,5	120,5	127,5	122,5	10 (10)	15 (15)	=	55

¹⁾ Gearheads with ratio $\geq 14:1$ have plastic gears in the input stage. For extended life performance, the gearheads are available with all steel gears and heavy duty lubricant as type 38/1 S and 38/2 S.

The values for the torque rating indicated in parenthesis, are for gearheads, type 38/1 S and 38/2 S with all steel gears.

²⁾ Planetary Gearhead, series 38/1

Note: The reduction ratios are rounded, the exact values are available on request.



For details on technical information and lifetime performance refer to pages 104-108.

Edition 2006-2007

Specifications subject to change without notice.

www.faulhaber-group.com

Encoders

Magnetic Encoders

Features:
 64 to 512 Lines per revolution
 2 Channels
 Digital output

Series IE2 – 512

	IE2 – 64	IE2 – 128	IE2 – 256	IE2 – 512	
Lines per revolution	N	64	128	256	512
Signal output, square wave		2			channels
Supply voltage	V _{DD}	4,5 ... 5,5			V DC
Current consumption, typical (V _{DD} = 5 V DC)	I _{DD}	typ. 6, max. 12			mA
Output current, max. ¹⁾	I _{OUT}	5			mA
Pulse width	P	180 ± 45			°e
Phase shift, channel A to B	Φ	90 ± 45			°e
Signal rise/fall time, max. (C _{LOAD} = 50 pF)	tr/tf	0,1 / 0,1			μs
Frequency range ²⁾ , up to	f	20	40	80	160
Inertia of code disc ³⁾	J	0,09			kgcm ²
Operating temperature range		- 25 ... + 85			°C

¹⁾ V_{DD} = 5 V DC; Low logic level < 0,5 V, high logic level > 4,5 V: CMOS and TTL compatible

²⁾ Velocity (rpm) = f (Hz) × 60/N

³⁾ For the brushless DC-Servomotors 1628 ... B, 2036 ... B and 2444 ... B the inertia of code disc is J = 0,14 gcm²

Ordering information

Encoder	number of channels	lines per revolution	in combination with:
IE2 – 64	2	64	DC-Micromotors series
IE2 – 128	2	128	1336 ... C, 1516 ... SR, 1524 ... SR,
IE2 – 256	2	256	1717 ... SR, 1724 ... SR, 1727 ... C, 2224 ... SR, 2232 ... SR, 2342 ... CR,
IE2 – 512	2	512	2642 ... CR, 2657 ... CR, 3242 ... CR, 3257 ... CR, 3863 ... C
			Brushless DC-Servomotors series 1628 ... B, 2036 ... B, 2057 ... B, 2444 ... B

Features

These incremental shaft encoders in combination with the FAULHABER DC-Micromotors and Brushless DC-Servomotors are used for indication and control of both shaft velocity and direction of rotation as well as for positioning.

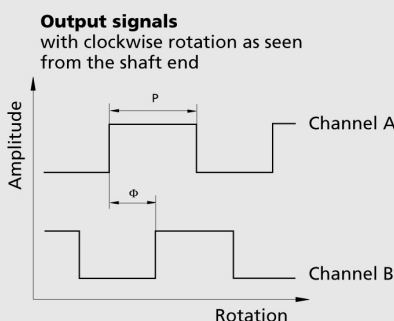
The encoder is integrated in the DC-Micromotors SR-Series and extends the overall length by only 1,4 mm. Built-on option for DC-Micromotors and Brushless DC-Servomotors.

Hybrid circuits with sensors and a low inertia magnetic disc provide two channels with 90° phase shift.

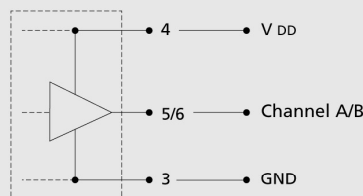
The supply voltage for the encoder and the DC-Micromotor as well as the two channel output signals are interfaced through a ribbon cable with connector.

Details for the DC-Micromotors and suitable reduction gearheads are on separate catalogue pages.

Output signals / Circuit diagram / Connector information



Output circuit

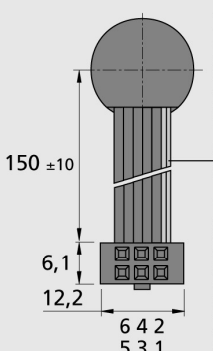


Pin Function

- 1 Motor – *
- 2 Motor + *
- 3 GND
- 4 V_{DD}
- 5 channel B
- 6 channel A

PVC-Ribbon cable

6 conductors 0,09 mm²



Note: The terminal resistance of all motors with precious metal commutation is increased by approx. 0.4 Ω, and the max. allowable motor current in combination is 1A. Motors with graphite commutation and brushless motors have separate motor leads and higher motor current is allowed.

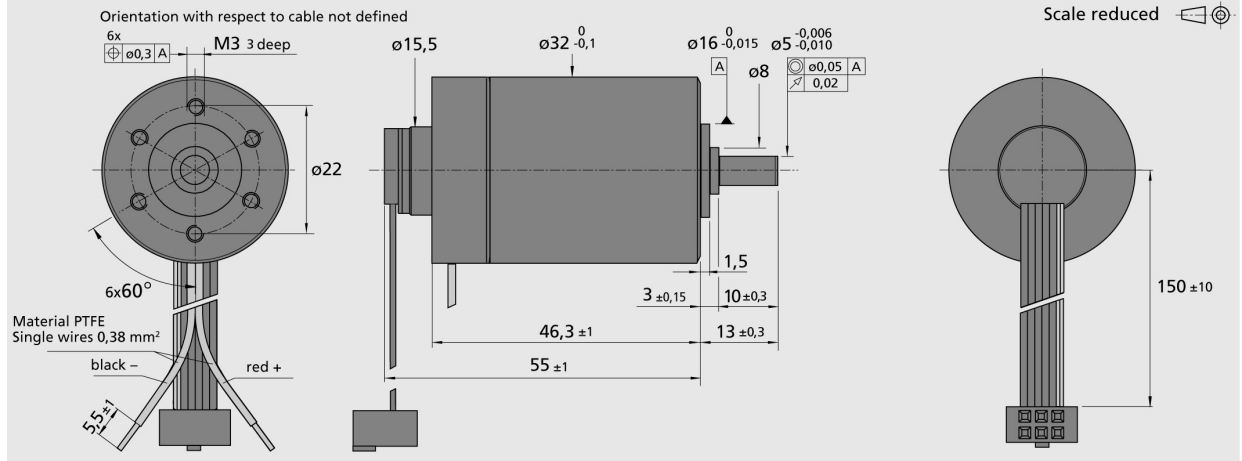
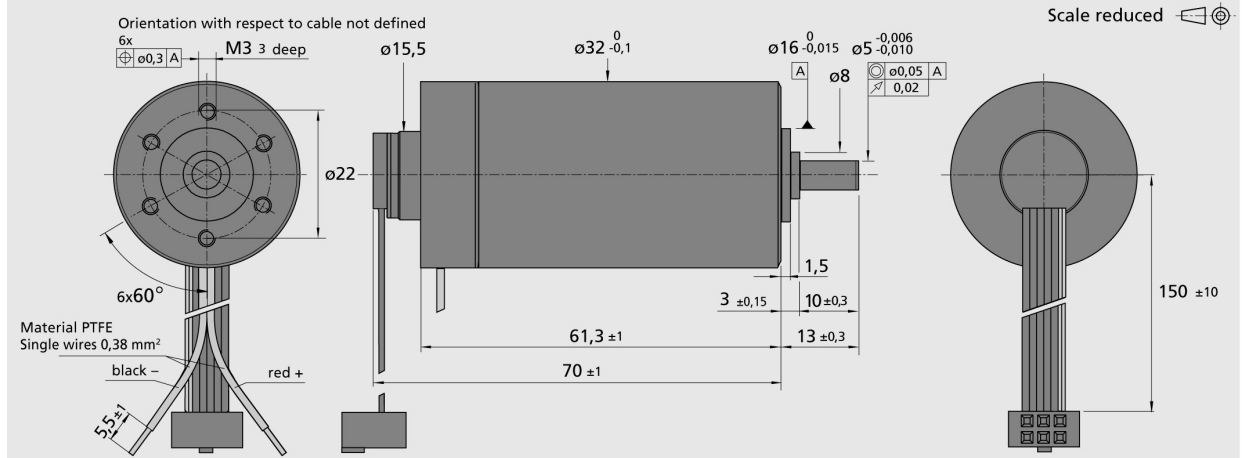
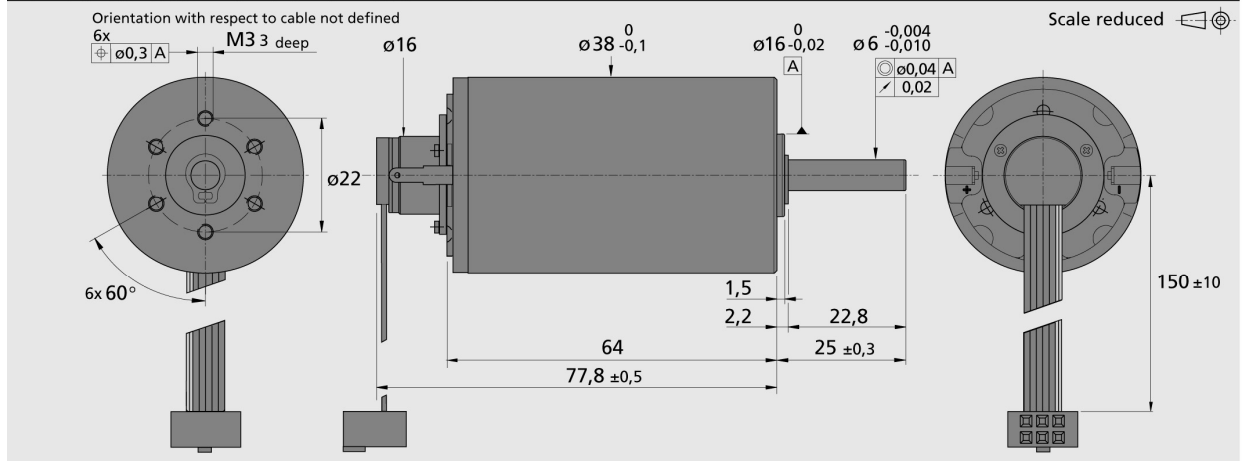
Connector
DIN-41651
grid 2,54 mm

For details on technical information and lifetime performance refer to pages 140-142.

Edition 2006-2007

Specifications subject to change without notice.

www.faulhaber-group.com

DC-Micromotor 3242 G ... CR with Encoder IE2 16 – 512

DC-Micromotor 3257 G ... CR with Encoder IE2 16 – 512

DC-Micromotor 3863 H ... C - 2016 with Encoder IE2 16 – 512


For details on technical information and lifetime performance
refer to pages 140-142.

Edition 2006-2007

Specifications subject to change without notice.

www.faulhaber-group.com

Appendix B: Electronic Components Datasheets

This section contains the title page of the datasheets of the electronics components that were used for the main microcontroller / IMU board, the H-bridges, and the Motor Driver board.

The following ICs were used:

1. Freescale MAC7121 - 32bit ARM7 microcontroller
2. Texas Instruments TPS73633 - 400mA Low Noise 3.3V LDO linear voltage regulator
3. Texas Instruments TPS73250 - 250mA Low Noise 5.0V LDO linear voltage regulator
4. MaxStream XBee Pro Zigbee module
5. Analog Devices ADIS16250 - SPI Out $\pm 320^\circ/\text{s}$ MEMS Gyroscope
6. Analog Devices ADIS16201 - SPI Out Dual Axis Accelerometer / Inclinometer
7. Texas Instruments TPS2836 - MOSFET Driver with TTL Inputs
8. Texas Instruments PTN7800W - 1.5-A Wide-Input Adjustable Switching Regulator
9. ON Semiconductor NTD70N03R - 72 A, 25 V, N-Channel MOSFET's

MAC71x1 Microcontroller Device Product Brief

Covers MAC7101, MAC7111, MAC7121, MAC7131, MAC7141

32-bit Embedded Controller Division

MAC71x1 microcontrollers (MCUs) are members of a pin-compatible family of 32-bit Flash-memory-based devices developed specifically for embedded automotive applications. The pin-compatible family concept enables users to select between different memory and peripheral options for scalable designs. All MAC71x1 devices are composed of an ARM7TDMI-S™ 32-bit central processing unit, 512 Kbytes of high performance embedded Flash memory for program storage, an optional 32 Kbytes of embedded Flash for data and/or program storage, and 32 Kbytes of RAM.

As shown in [Table 1](#) and [Figure 1](#), the MAC71x1 family is implemented with a variety of on-chip peripherals. An enhanced DMA (eDMA) controller executes in parallel with the CPU to improve the performance of data transfers between memory and many of the peripherals. DMA transfers may be triggered by various peripheral events, such as data frame transmission or reception, elapsed timer periods, and analog-to-data conversion completions. The peripheral set includes enhanced asynchronous serial communications interfaces (eSCI) with Local Interconnect Network (LIN) support hardware to reduce interrupt overhead, serial peripheral interfaces (DSPI) with flexible chip selects and fast baud

Table of Contents

1	Block Diagram.....	3
2	Features.....	3
3	Modes of Operation	8
3.1	Chip Configuration Modes	8
3.2	Low-Power Modes	9
4	Functional Overview	9
4.1	32-bit ARM7TDMI-S RISC Core.....	9
4.2	Enhanced Direct Memory Access (eDMA) and Channel Multiplexer (DMA MUX)	9
4.3	External Interface Module (EIM).....	10
4.4	Common Flash Module (CFM)	10
4.5	Interrupt Controller (INTC).....	10
4.6	Port Integration Module (PIM)	10
4.7	Analog-to-Digital Converters (ATD)	11
4.8	CAN 2.0 Software Compatible (FlexCAN) Modules.....	11
4.9	Enhanced Modular I/O Subsystem (eMIOS)....	12
4.10	Serial Peripheral Interfaces (DSPI)	12
4.11	Enhanced Serial Communications Interfaces (eSCI)	12
4.12	Inter-Integrated Circuit (I ² C) Bus Module	13
4.13	Periodic Interrupt Timer (PIT) Module	13
4.14	Miscellaneous Control Module (MCM) and Cross-Bar Switch (XBS)	13
4.15	System Services Module (SSM).....	14
4.16	Voltage Regulator Module (VREG).....	14
4.17	System Clocks (OSC and CRG).....	14
4.18	Development Support.....	14
5	Documentation and Ordering.....	15



This document contains information on a new product. Specifications and information herein are subject to change without notice.

© Freescale Semiconductor, Inc., 2004. All rights reserved.

• Preliminary



Table 1. MAC71x1 Device Derivatives

	MAC7101	MAC7111	MAC7121	MAC7131	MAC7141
Program Flash	512 Kbytes				
Data Flash	32 Kbytes				
SRAM	32 Kbytes				
External Bus	—	Yes	—	Yes	—
ATD Modules ⁽¹⁾	A	Yes	Yes	Yes	Yes
	B	Yes	—	Yes	—
CAN Modules	A	Yes	Yes	Yes	Yes
	B	Yes	Yes	Yes	Yes
	C	Yes	Yes	Yes	—
	D	Yes	Yes	Yes	—
eSCI Modules	A	Yes	Yes	Yes	Yes
	B	Yes	Yes	Yes	Yes
	C	Yes	Yes	Yes	—
	D	Yes	Yes	Yes	Yes
DSPI Modules	A	Yes	Yes	Yes	Yes
	B	Yes	Yes	Yes ⁽²⁾	Yes
I ² C Module	Yes	Yes	Yes	Yes	Yes
eMIOS Module	16 channels, 16-bit				
Timer Module	10 channels, 24-bit				
GPIO Pins (max.) ⁽³⁾	112	112	85	128	72
Package	144 LQFP	144 LQFP	112 LQFP	208 MAP BGA	100 LQFP

NOTES:

1. 16 channels, 8/10-bit, per module.
2. Only three chip select signals available.
3. Early mask set devices (L49P) reduce these values by one.

rate switching, inter-integrated circuit (I²CTM) bus controllers, FlexCAN interfaces with flexible message buffering, an enhanced modular I/O subsystem (eMIOS) with sixteen high-performance 16-bit timers, one or two sixteen-channel 10-bit analog-to-digital converters (ATD), general-purpose timers (Programmable Interrupt Timer (PIT)) and two special-purpose timers (Real Time Interrupt (RTI) and Software Watchdog Timer (SWT)). The peripherals share a large number of general purpose input-output (GPIO) pins, all of which are bidirectional and available with interrupt capability to trigger wake-up from low-power chip modes.

Internal data paths between the CPU core, eDMA, memory and peripherals are all 32 bits wide, further improving performance for 32-bit applications. The MAC7111 and MAC7131 also offer a 16-bit wide external data bus with 22 address lines, allowing access of up to 4 MBytes of external address space. The inclusion of a programmable PLL module allows power consumption and performance to be adjusted to suit operational requirements. Both E-ICE and Nexus 2 interfaces are implemented to support development and debug tool chains.

MAC71x1 devices include an on-chip multi-output voltage regulator, thus requiring only a single external 3.3V to 5V power supply. The maximum operating range of devices in the family covers a junction temperature of -40° C to 150° C and CPU clock frequencies up to 50 MHz (below 105° C, frequency is limited to 40 MHz @ 150° C). Packaging options range from 100-pin LQFP up to 208-pin MAP BGA.



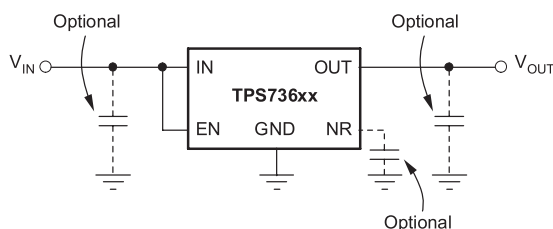
Cap-Free, NMOS, 400mA Low-Dropout Regulator with Reverse Current Protection

FEATURES

- Stable with No Output Capacitor or Any Value or Type of Capacitor
- Input Voltage Range of 1.7V to 5.5V
- Ultra-Low Dropout Voltage: 75mV typ
- Excellent Load Transient Response—with or without Optional Output Capacitor
- New NMOS Topology Delivers Low Reverse Leakage Current
- Low Noise: 30 μ V_{RMS} typ (10Hz to 100kHz)
- 0.5% Initial Accuracy
- 1% Overall Accuracy Over Line, Load, and Temperature
- Less Than 1 μ A max I_Q in Shutdown Mode
- Thermal Shutdown and Specified Min/Max Current Limit Protection
- Available in Multiple Output Voltage Versions
 - Fixed Outputs of 1.20V to 5.0V
 - Adjustable Output from 1.20V to 5.5V
 - Custom Outputs Available

APPLICATIONS

- Portable/Battery-Powered Equipment
- Post-Regulation for Switching Supplies
- Noise-Sensitive Circuitry such as VCOs
- Point of Load Regulation for DSPs, FPGAs, ASICs, and Microprocessors

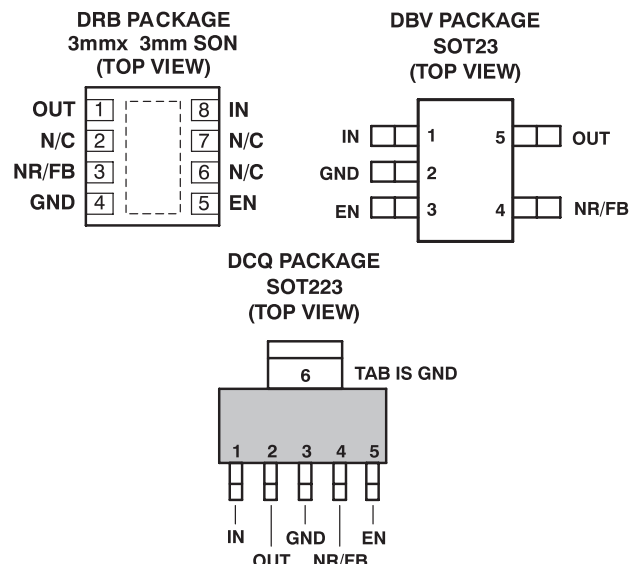


Typical Application Circuit for Fixed Voltage Versions

DESCRIPTION

The TPS736xx family of low-dropout (LDO) linear voltage regulators uses a new topology: an NMOS pass element in a voltage-follower configuration. This topology is stable using output capacitors with low ESR, and even allows operation without a capacitor. It also provides high reverse blockage (low reverse current) and ground pin current that is nearly constant over all values of output current.

The TPS736xx uses an advanced BiCMOS process to yield high precision while delivering very low dropout voltages and low ground pin current. Current consumption, when not enabled, is under 1 μ A and ideal for portable applications. The extremely low output noise (30 μ V_{RMS} with 0.1 μ F C_{NR}) is ideal for powering VCOs. These devices are protected by thermal shutdown and foldback current limit.



Please be aware that an important notice concerning availability, standard warranty, and use in critical applications of Texas Instruments semiconductor products and disclaimers thereto appears at the end of this data sheet.

All trademarks are the property of their respective owners.



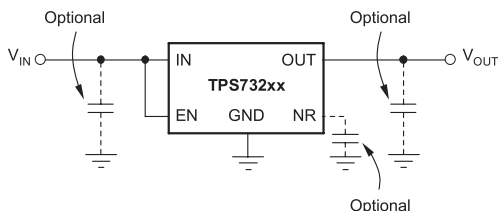
Cap-Free, NMOS, 250mA Low Dropout Regulator with Reverse Current Protection

FEATURES

- Stable with No Output Capacitor or Any Value or Type of Capacitor
- Input Voltage Range: 1.7V to 5.5V
- Ultralow Dropout Voltage: 40mV Typ at 250mA
- Excellent Load Transient Response—with or without Optional Output Capacitor
- New NMOS Topology Provides Low Reverse Leakage Current
- Low Noise: 30 μ V_{RMS} Typ (10kHz to 100kHz)
- 0.5% Initial Accuracy
- 1% Overall Accuracy (Line, Load, and Temperature)
- Less Than 1 μ A Max I_Q in Shutdown Mode
- Thermal Shutdown and Specified Min/Max Current Limit Protection
- Available in Multiple Output Voltage Versions
 - Fixed Outputs of 1.20V to 5.0V
 - Adjustable Outputs from 1.20V to 5.5V
 - Custom Outputs Available

APPLICATIONS

- Portable/Battery-Powered Equipment
- Post-Regulation for Switching Supplies
- Noise-Sensitive Circuitry such as VCOs
- Point of Load Regulation for DSPs, FPGAs, ASICs, and Microprocessors

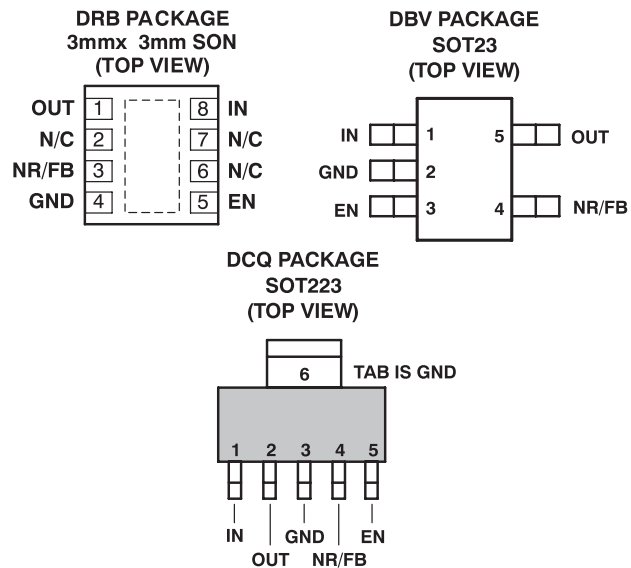


Typical Application Circuit for Fixed-Voltage Versions

DESCRIPTION

The TPS732xx family of low-dropout (LDO) voltage regulators uses a new topology: an NMOS pass element in a voltage-follower configuration. This topology is stable using output capacitors with low ESR, and even allows operation without a capacitor. It also provides high reverse blockage (low reverse current) and ground pin current that is nearly constant over all values of output current.

The TPS732xx uses an advanced BiCMOS process to yield high precision while delivering very low dropout voltages and low ground pin current. Current consumption, when not enabled, is under 1 μ A and ideal for portable applications. The extremely low output noise (30 μ V_{RMS} with 0.1 μ F C_{NR}) is ideal for powering VCOs. These devices are protected by thermal shutdown and foldback current limit.

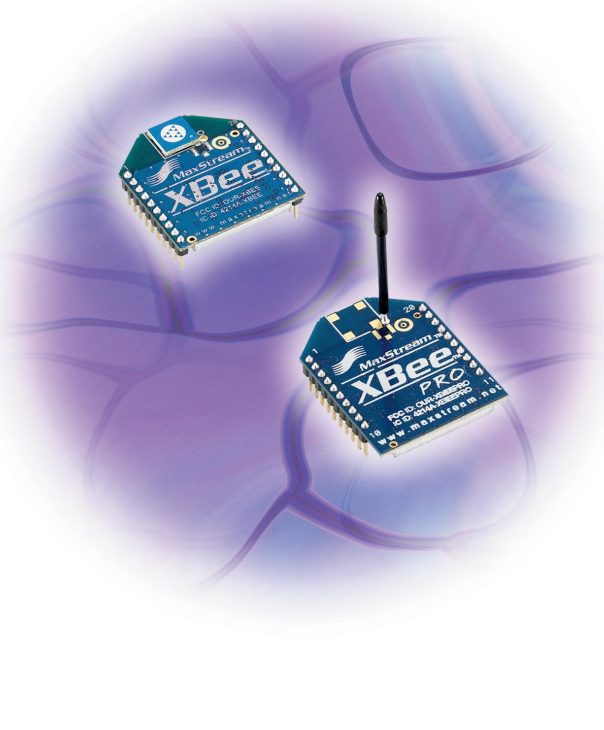


Please be aware that an important notice concerning availability, standard warranty, and use in critical applications of Texas Instruments semiconductor products and disclaimers thereto appears at the end of this data sheet.

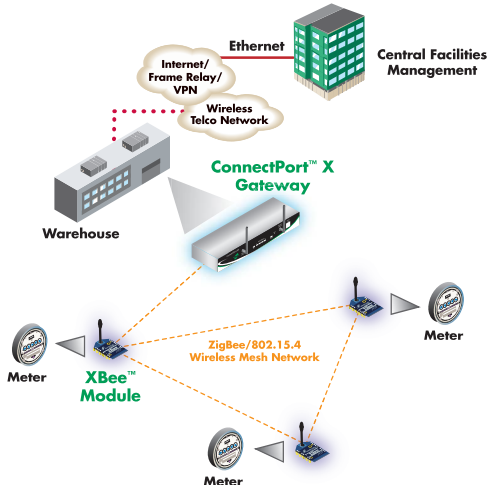
All trademarks are the property of their respective owners.

XBee™ ZigBee®/802.15.4 Modules

2.4 GHz OEM RF Modules



Part of Digi's Drop-in Networking product family, XBee OEM RF modules provide reliable, wireless data communication over ZigBee/802.15.4 networks. Available in Series 1 or Series 2 models for point-to-multipoint or mesh topologies, they enable OEMs with excellent wireless performance in a cost-effective, small form factor solution.



Features/Benefits

- ZigBee/802.15.4 compatible RF modules
- 2.4 GHz ISM band for use worldwide
- Fully interoperable with other Digi Drop-in Networking products, including gateways, device adapters and extenders
- Available in Series 1 or Series 2 models for point-to-multipoint or mesh topologies
- Pin-swappable regular and long-range -PRO versions
- Low cost
- Common footprint for a variety of Digi RF modules
- Low-power sleep modes
- Multiple antenna options
- Industrial temperature (-40° C to 85° C)

Overview

The XBee family of ZigBee/802.15.4 RF modules is the premiere choice for OEMs looking for excellent wireless performance in a cost-effective, small form factor solution. Each XBee module comes in either a regular or long-range “-PRO” version*. All XBee modules are pin-for-pin compatible with the exception of a few varying I/O features, which provides a standard footprint for OEMs with multiple applications.

XBee Series 1 is based on ZigBee/802.15.4 silicon from Freescale®. Its 802.15.4 firmware feature set makes it ideal for point-to-point, peer-to-peer, and point-to-multipoint (star) topologies. The XBee Series 1 gives the user maximum control over network nodes and minimum latency.

XBee Series 2 is based on ZigBee/802.15.4 silicon from Ember™. It features ZigBee firmware for creating ad-hoc mesh networks. The XBee Series 2 performs automatic route discoveries to create a self-healing network of full-function routers and low-power end devices. XBee Series 1 and Series 2 modules do not communicate with one another.

Known for ease of use, the XBee modules are ready to operate out of the box and offer simple AT commands or an API for advanced, user-settable configurations. XBee modules are recognized worldwide for reliable wireless data communication in the license-free 2.4 GHz ISM band. Visit our website for a complete listing of countries that have approved the XBee as a certified, license-free RF module with no need for further testing.

XBee modules are a part of Digi's full line of Drop-in Networking products. ConnectPort X gateways and XBee device adapters, modules and extenders provide end-to-end wireless connectivity to commercial-grade electronic devices in locations where wired infrastructure does not exist or satisfy customer needs. To learn more about Drop-in Networking, visit www.digi.com/products/wirelessdropinnetworking.

FEATURES

Yaw rate gyroscope with digital range scaling
 $\pm 80^\circ/\text{sec}$, $\pm 160^\circ/\text{sec}$, and $\pm 320^\circ/\text{sec}$ settings

14-bit digital gyroscope sensor outputs

12-bit digital temperature sensor output

Calibrated sensitivity and bias

- ADIS16250: $+25^\circ\text{C}$
- ADIS16255: -40°C to $+85^\circ\text{C}$

In-system, auto-zero for bias drift calibration

Digitally controlled sample rate

Digitally controlled frequency response

Dual alarm settings with configurable operation

Embedded integration for short-term angle estimates

Digitally activated self-test

Digitally activated low power mode

- Interrupt-driven wake-up

SPI®-compatible serial interface

50 Hz sensor bandwidth

Auxiliary 12-bit ADC input and 12-bit DAC output

Auxiliary digital input/output

Single-supply operation: 4.75 V to 5.25 V

2000 g powered shock survivability

APPLICATIONS

Instrumentation control
Platform control and stabilization
Motion control and analysis
Avionics instrumentation
Navigation
Image stabilization
Robotics

FUNCTIONAL BLOCK DIAGRAM

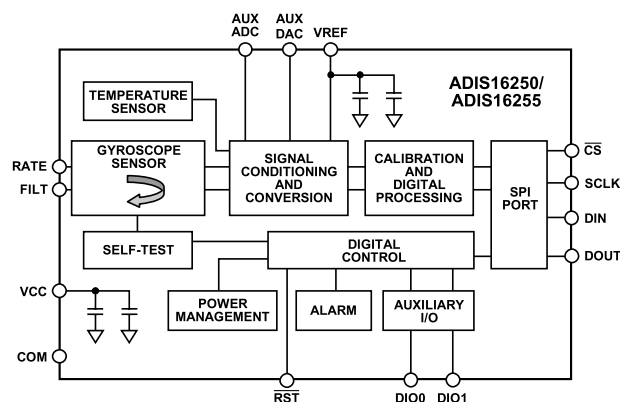


Figure 1.

08070001

GENERAL DESCRIPTION

The ADIS16250/ADIS16255 are complete angular rate measurement systems available in a single compact package enabled by Analog Devices, Inc. *iSensor™* integration. By enhancing Analog Devices *iMEMS®* sensor technology with an embedded signal processing solution, the ADIS16250/ADIS16255 provide factory-calibrated and tunable digital sensor data in a convenient format that can be accessed using a simple SPI serial interface. The ADIS16255 additionally provides an extended temperature calibration. The SPI interface provides access to measurements for the gyroscope, temperature, power supply, and one auxiliary analog input. Easy access to calibrated digital sensor data provides developers with a system-ready device, reducing development time, cost, and program risk.

The device range can be digitally selected from three different settings: $\pm 80^\circ/\text{sec}$, $\pm 160^\circ/\text{sec}$, and $\pm 320^\circ/\text{sec}$. Unique characteristics of the end system are accommodated easily through

several built-in features, including a single-command auto-zero recalibration function, as well as configurable sample rate and frequency response. Additional features can be used to further reduce system complexity, including:

- Configurable alarm function
- Auxiliary 12-bit ADC and DAC
- Two configurable digital I/O ports
- Digital self-test function

System power dissipation can be optimized via the ADIS16250/ADIS16255 power management features, including an interrupt-driven wake-up. The ADIS16250/ADIS16255 are available in an 11 mm × 11 mm × 5.5 mm, laminate-based land grid array (LGA) package with a temperature range of -40°C to $+85^\circ\text{C}$.

Rev. B

Information furnished by Analog Devices is believed to be accurate and reliable. However, no responsibility is assumed by Analog Devices for its use, nor for any infringements of patents or other rights of third parties that may result from its use. Specifications subject to change without notice. No license is granted by implication or otherwise under any patent or patent rights of Analog Devices. Trademarks and registered trademarks are the property of their respective owners.

FEATURES

Dual-axis inclinometer/accelerometer measurements
12-, 14-bit digital inclination/acceleration sensor outputs
 $\pm 1.7\text{ g}$ accelerometer measurement range
 $\pm 90^\circ$ inclinometer measurement range, linear output
12-bit digital temperature sensor output
Digitally controlled sensitivity and bias calibration
Digitally controlled sample rate
Digitally controlled frequency response
Dual alarm settings with rate/threshold limits
Auxiliary digital I/O
Digitally activated self test
Digitally activated low power mode
SPI®-compatible serial interface
Auxiliary 12-bit ADC input and DAC output
Single-supply operation: 3.0 V to +3.6 V
3500 g powered shock survivability

FUNCTIONAL BLOCK DIAGRAM

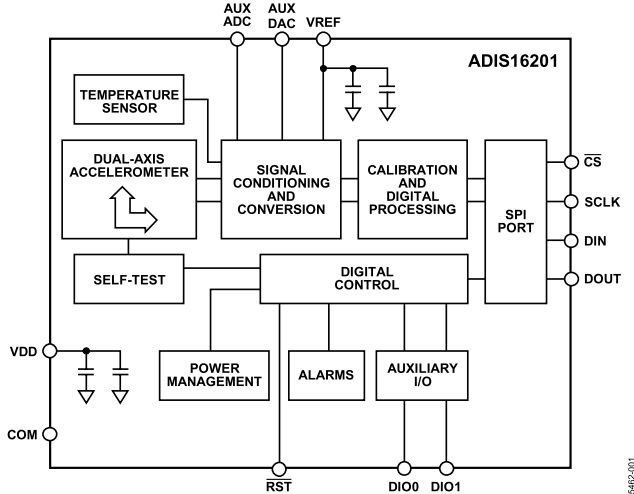


Figure 1.

05462-001

APPLICATIONS

Platform control, stabilization, and leveling
Tilt sensing, inclinometers
Motion/position measurement
Monitor/alarm devices (security, medical, safety)

GENERAL DESCRIPTION

The ADIS16201 is a complete, dual-axis acceleration and inclination angle measurement system available in a single compact package enabled by the Analog Devices iSensor™ integration. By enhancing the Analog Devices iMEMS® sensor technology with an embedded signal processing solution, the ADIS16201 provides factory calibrated and tunable digital sensor data in a convenient format that can be accessed using a serial peripheral interface (SPI). The SPI interface provides access to measurements for dual-axis linear acceleration, dual-axis linear inclination angle, temperature, power supply, and one auxiliary analog input. Easy access to calibrated digital sensor data provides developers with a system-ready device, reducing development time, cost, and program risk.

Unique characteristics of the end system are accommodated easily through several built-in features, such as a single command in-system offset calibration, along with convenient sample rate and bandwidth control.

The ADIS16201 offers the following embedded features, which eliminate the need for external circuitry and provide a simplified system interface:

- Configurable alarm function
- Auxiliary 12-bit ADC
- Auxiliary 12-bit DAC
- Configurable digital I/O port
- Digital self-test function

The ADIS16201 offers two power management features for managing system-level power dissipation: low power mode and a configurable shutdown feature.

The ADIS16201 is available in a 9.2 mm × 9.2 mm × 3.9 mm laminate-based land grid array (LGA) package with a temperature range of -40°C to $+125^\circ\text{C}$.

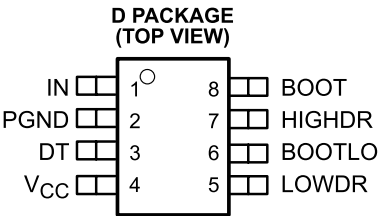
Rev. A

Information furnished by Analog Devices is believed to be accurate and reliable. However, no responsibility is assumed by Analog Devices for its use, nor for any infringements of patents or other rights of third parties that may result from its use. Specifications subject to change without notice. No license is granted by implication or otherwise under any patent or patent rights of Analog Devices. Trademarks and registered trademarks are the property of their respective owners.

TPS2836, TPS2837
SYNCHRONOUS-BUCK MOSFET DRIVER
WITH DEAD-TIME CONTROL

SLVS224B – NOVEMBER 1999 – REVISED AUGUST 2002

- Floating Bootstrap or Ground-Reference High-Side Driver
- Adaptive Dead-Time Control
- 50-ns Max Rise/Fall Times With 3.3-nF Load
- 2.4-A Typical Output Current
- 4.5-V to 15-V Supply Voltage Range
- TTL-Compatible Inputs
- Internal Schottky Bootstrap Diode
- Low Supply Current....3 mA Typical
- Ideal for High-Current Single or Multiphase Power Supplies
- – 40°C to 125°C Operating Virtual Junction-Temperature Range



description

The TPS2836 and TPS2837 are MOSFET drivers for synchronous-buck power stages. These devices are ideal for designing a high-performance power supply using switching controllers that do not have MOSFET drivers. The drivers are designed to deliver minimum 2-A peak currents into large capacitive loads. The high-side driver can be configured as ground-reference or as floating-bootstrap. An adaptive dead-time control circuit eliminates shoot-through currents through the main power FETs during switching transitions and provides high efficiency for the buck regulator.

The TPS2836 has a noninverting input, while the TPS2837 has an inverting input. These drivers, available in 8-terminal SOIC packages, operate over a junction temperature range of – 40°C to 125°C.

AVAILABLE OPTIONS

T _J	PACKAGED DEVICES	
	SOIC (D)	
– 40°C to 125°C	TPS2836D TPS2837D	

The D package is available taped and reeled. Add R suffix to device type (e.g., TPS2836DR)

Related Synchronous MOS FET Drivers

DEVICE NAME	ADDITIONAL FEATURES	INPUTS	
TPS2830	ENABLE, SYNC and CROWBAR	CMOS	Noninverted
TPS2831			Inverted
TPS2832	W/O ENABLE, SYNC and CROWBAR	CMOS	Noninverted
TPS2833			Inverted
TPS2834	ENABLE, SYNC and CROWBAR	TTL	Noninverted
TPS2835			Inverted



Please be aware that an important notice concerning availability, standard warranty, and use in critical applications of Texas Instruments semiconductor products and disclaimers thereto appears at the end of this data sheet.

PRODUCTION DATA information is current as of publication date. Products conform to specifications per the terms of Texas Instruments standard warranty. Production processing does not necessarily include testing of all parameters.

Copyright © 2002, Texas Instruments Incorporated



POST OFFICE BOX 655303 • DALLAS, TEXAS 75265

1.5-A, WIDE-INPUT ADJUSTABLE SWITCHING REGULATOR

FEATURES

- 1.5-A Output Current
- Wide-Input Voltage
(7 V to 36 V) / (15 V to 36 V)
- Wide-Output Voltage Adjust
(2.5 V to 12.6 V) / (11.85 V to 22 V)
- High Efficiency (Up to 95%)
- On/Off Inhibit
- Undervoltage Lockout
- Output Current Limit
- Overtemperature Shutdown
- Operating Temperature: -40°C to 85°C
- Surface Mount Package Available

APPLICATIONS

- General-Purpose, Industrial Controls, HVAC Systems, Test and Measurement, Medical Instrumentation, AC/DC Adaptors, Vehicles, Marine, and Avionics

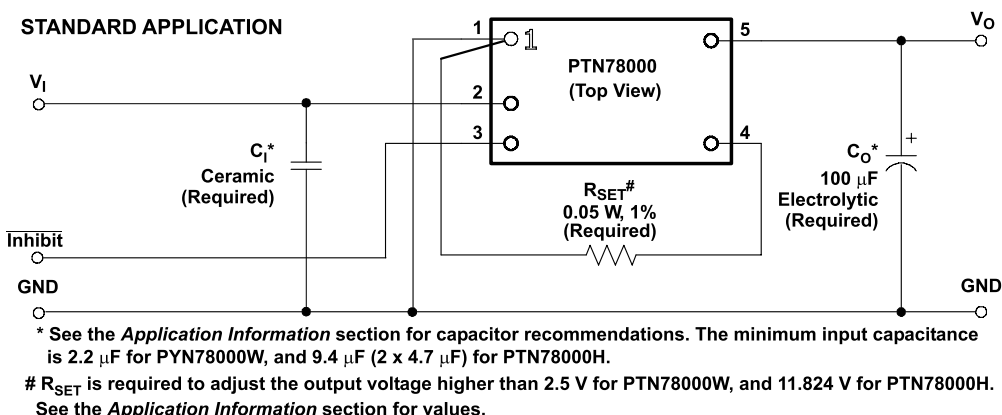


DESCRIPTION

The PTN78000 is a series of high-efficiency, step-down Integrated Switching Regulators (ISR), that represent the third generation in the evolution of the popular 78ST100 series of products. In new designs it should be considered in place of the 78ST100, PT78ST100, PT5100, and PT6100 series of single in-line pin (SIP) products. The PTN78000 is smaller and lighter than its predecessors, and has either similar or improved electrical performance characteristics. The case-less, double-sided package, also exhibits improved thermal characteristics, and is compatible with TI's roadmap for RoHS and lead-free compliance.

Operating from a wide-input voltage range, the PTN78000 provides high-efficiency, step-down voltage conversion for loads of up to 1.5 A. The output voltage is set using a single external resistor. The PTN78000W may be set to any value within the range, 2.5 V to 12.6 V, and the PTN78000H from 11.85 V to 22 V. The output voltage of the PTN78000W can be as little as 2 V lower than the input, allowing operation down to 7 V, with an output voltage of 5 V. The output voltage of the PTN78000H can be as little as 3 V lower than the input, allowing operation down to 15 V, with an output voltage of 12 V.

The PTN78000 has undervoltage lockout and an integral on/off inhibit. The modules are suited to a wide variety of general-purpose applications that operate off 12-V, 24-V, or 28-V dc power.



Please be aware that an important notice concerning availability, standard warranty, and use in critical applications of Texas Instruments semiconductor products and disclaimers thereto appears at the end of this data sheet.

NTD70N03R

Power MOSFET

72 A, 25 V, N-Channel DPAK

Features

- Planar HD3e Process for Fast Switching Performance
- Low $R_{DS(on)}$ to Minimize Conduction Loss
- Low C_{ISS} to Minimize Driver Loss
- Low Gate Charge
- Pb-Free Packages are Available

MAXIMUM RATINGS ($T_J = 25^\circ\text{C}$ Unless otherwise specified)

Parameter	Symbol	Value	Unit
Drain-to-Source Voltage	V_{DSS}	25	V_{dc}
Gate-to-Source Voltage – Continuous	V_{GS}	± 20	V_{dc}
Thermal Resistance – Junction-to-Case Total Power Dissipation @ $T_C = 25^\circ\text{C}$	$R_{\theta JC}$ P_D	2.4 62.5	$^\circ\text{C}/\text{W}$ W
Drain Current – Continuous @ $T_C = 25^\circ\text{C}$, Chip – Continuous @ $T_C = 25^\circ\text{C}$, Limited by Package – Continuous @ $T_A = 25^\circ\text{C}$, Limited by Wires – Single Pulse ($t_p = 10 \mu\text{s}$)	I_D I_D I_D I_{DM}	72.0 62.8 32 140	A A A A
Thermal Resistance – Junction-to-Ambient (Note 1) Total Power Dissipation @ $T_A = 25^\circ\text{C}$	$R_{\theta JA}$ P_D	80 1.87	$^\circ\text{C}/\text{W}$ W
Drain Current – Continuous @ $T_A = 25^\circ\text{C}$	I_D	12.0	A
Thermal Resistance – Junction-to-Ambient (Note 2) Total Power Dissipation @ $T_A = 25^\circ\text{C}$	$R_{\theta JA}$ P_D	110 1.36	$^\circ\text{C}/\text{W}$ W
Drain Current – Continuous @ $T_A = 25^\circ\text{C}$	I_D	10.0	A
Operating and Storage Temperature Range	T_J, T_{stg}	-55 to 175	$^\circ\text{C}$
Single Pulse Drain-to-Source Avalanche Energy – Starting $T_J = 25^\circ\text{C}$ ($V_{DD} = 30 \text{ V}_{dc}$, $V_{GS} = 10 \text{ V}_{dc}$, $I_L = 12 \text{ A}_{pk}$, $L = 1 \text{ mH}$, $R_G = 25 \Omega$)	E_{AS}	71.7	mJ
Maximum Lead Temperature for Soldering Purposes, 1/8" from Case for 10 s	T_L	260	$^\circ\text{C}$

Stresses exceeding Maximum Ratings may damage the device. Maximum Ratings are stress ratings only. Functional operation above the Recommended Operating Conditions is not implied. Extended exposure to stresses above the Recommended Operating Conditions may affect device reliability.

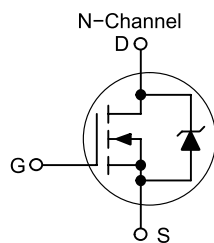
1. When surface mounted to an FR4 board using 0.5 sq. in. pad size.
2. When surface mounted to an FR4 board using minimum recommended pad size.



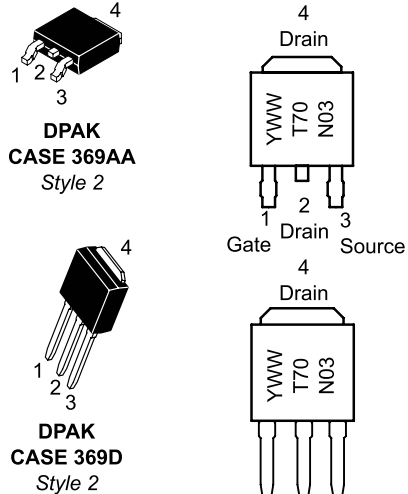
ON Semiconductor®

<http://onsemi.com>

$V_{(BR)DSS}$	$R_{DS(on)} \text{ TYP}$	$I_D \text{ MAX}$
25 V	5.6 mΩ	72 A



MARKING DIAGRAMS



70N03 Device Code
Y = Year
WW = Work Week

ORDERING INFORMATION

See detailed ordering and shipping information in the package dimensions section on page 6 of this data sheet.

Appendix C: MAC71xx Development Tool Chain

The MAC71xx Development Tool Chain is comprised of the following tools:

1. IAR Embedded Workbench 32KB Kickstart Edition for the ARM
The IAR IDE includes C and C++ compilers, along with an ARM Assembler and Linker. The IDE comes with Header files for the SFR definitions for the MAC71xx family. Also included with the IDE is a simulator. It also supports a variety of debug interfaces, including the official Macraigor Wiggler interface, and support for third-party RDI interfaces. IAR comes equipped with bootloaders to burn code onto the FLASH memory, and to perform In-Circuit Debugging via the JTAG interface.
2. H-JTAG RDI Server
The H-JTAG RDI Server provides a way for IAR to use third party debug interfaces via the standard RDI 1.5 protocol. In this case, H-JTAG is configured to use the wiggler clone via the parallel port as the debug interface.
3. Wiggler Clone
Wiggler is a simple parallel port JTAG interface first introduced by Macraigor Systems. Unfortunately, the Macraigor drivers for the latest wiggler interface are quite slow, and the newer versions have a hardware lock to prevent them from being cloned. Therefore, a clone of the first version of the wiggler board is used along with the H-JTAG drivers.

Appendix D: Source Code

Mathematica Source Code for the simulation of a reaction wheel inverted pendulum

```
Motor Parameters;
V = 24;
reduction = 14;
efficiency = 0.8;
Ke = 3.95 / 1000 / (2 * Pi) * 60 * reduction / efficiency
Ki = 0.027 * 1000 / reduction
J = 1 * 0.775^2;
R = 1.63;

Motor Equations;
DSolve[{V == Ke * w[t] + Ki * J * w'[t] * R, w[0] == 0.01}, w[t], t]
W =  $\frac{V}{Ke} \cdot \left(1 - e^{-\frac{Ke t}{J K i R}}\right)$ ;
Plot[W, {t, 0, 2}, PlotRange -> All]
Plot[(V - W * Ke) / R, {t, 0, 2}, PlotRange -> All, AxesOrigin -> {0, 0}]
Plot[((V - W * Ke) / R) / Ki * W, {t, 0, 2}, PlotRange -> All]
Dt[W, t];

Inverted Pendulum Equations;
Mb = 3;
Md = 1;
g = 9.8;
Rp = 1;
<< Graphics`Colors`;
DSolve[{(Md + Mb) * g * Rp * theta[t] == J * Dt[W, t] + theta''[t] * ((Mb + Md) * Rp^2), theta[0] == 10 °,
theta'[0] == 0}, theta[t], t]
Plot[theta[t] /. %, {t, 0, 2}, AxesOrigin -> {0, 0}, TextStyle -> {FontSize -> 22}];
Plot[((V - W * Ke) / (R * Ki), (Md + Mb) * g * Rp * Sin[theta[t] /. %%], (Md + Mb) * g * Rp * theta[t] /. %%), {t, 0, 2},
PlotRange -> All, PlotStyle -> {RGBColor[0, 0.8, 0], Red, Blue}, TextStyle -> {FontSize -> 22}]
```

MATLAB Source code for IMU Filter simulation

```
%=====
%      f = lowpass constant
%      dt = time step of digital filter
%      a = Complimentary filter inclinometer weight parameter
%=====
f=999/1000;
dt=0.0005;
a=0.0004/dt
T=f*dt/(1-f)
Optimal_a=(1-f)/(4*f*dt)
OptimalDigital_a=Optimal_a*dt
Digital_a=a*dt
numG=[T 1];
numA=[T*a a];
den=[T 1 a];
Gresponse=tf(numG,den);
Aresponse=tf(numA,den);
step(Gresponse, Aresponse)
```

Target Source Code

```
Module: Main.c
Main loop, IMU State Estimator Filter, Control Loop, Main 2KHz
Interrupt.

int main( void )
{
    Init();
    init_system();
    OnBoot();
    InitTransfers();

    DISABLE_BUZZER;

    while(1)
    {
        DebugDump();
        UpdateLED();
        processXBEE_readBuffer();
        BootCheck();
    }
}

void Filter()
{
    //=====IMU Filter and State Estimator=====
    X_Angle += X_Rate/2730 + 0.0004*(X_Angle_Incl-X_Angle_lp);
    Y_Angle += Y_Rate/2730 + 0.0004*(Y_Angle_Incl-Y_Angle_lp);
    Z_Angle += Z_Rate/2730;
    X_Angle_lp = (999*X_Angle_lp + X_Angle)/1000;
    X_Angle_Incl = (999*X_Angle_Incl + X_Incl)/1000;
    Y_Angle_lp = (999*Y_Angle_lp + Y_Angle)/1000;
    Y_Angle_Incl = (999*Y_Angle_Incl + Y_Incl)/1000;

    static unsigned short int en1=0, en2=0;
    if(en2>0x8000 && ENCODER2<0x4000)    //Overflow from 65535 to 0
    {
        RWENCODER = (RWENCODER + ((double)ENCODER2 +
                                (double)0x10000 - (double)en2))*0.9995;
    }
    else if(en2<0x4000 && ENCODER2>0x8000) //Overflow from 0 to 65535
    {
        RWENCODER = (RWENCODER + ((double)ENCODER2 -
                                (double)0x10000 - (double)en2))*0.9995;
    }
    else
    {
        RWENCODER = (RWENCODER + ((double)ENCODER2 -
                                (double)en2))*0.9995;
    }
    en2 = ENCODER2;

    DRENCODER = ENCODER1;
    //RWENCODER = ENCODER2;
    return;
}
```

```

void DoControlLoop()
{
    //=====The Main Control Loop=====
    if((TickCount%10)!=0)
        return;
#define kp 40.0
#define ki 0.1//0.0051
#define kd 1.0
#define kwp 0.0009
#define MAXSUM 100000.0

    errorsum = (errorsum + Y_Angle)*0.99;
    if(corrections>MAXSUM)
        corrections = MAXSUM;
    else if(corrections<-MAXSUM)
        corrections = -MAXSUM;

    corrections = kp*(Y_Angle-kwp*RWENCODER) + kd*Y_Rate +
                  ki*errorsum;

    if(corrections>400)
        corrections = 400;
    else if(corrections<-510)
        corrections = -510;

    RWMotor = 512.0 + corrections;
    return;
}

void MainInterrupt( void )
{
    PITFLG = BIT1; /* clear flag */
    TicksCount++;
    read_XBEE_RX_buf();
    ReadSensors();
    Filter();
    DoControlLoop();
    MotorControl();
    return;
}

```